SEMESTERARBEIT

Evaluation of impedance boundary conditions in ANSYS Fluent

Autor:
Michael Bertsch

Matrikel-No:
03640853

Betreuer:
Alexander Avdonin, M. Sc.
Prof. Wolfgang Polifke, Ph. D.

September 29, 2017

Technische Universität München
Fakultät für Maschinenwesen
Professur für Thermofluiddynamik
Prof. Wolfgang Polifke, Ph. D.

Erklärung

Hiermit versichere ich, die vorliegende Arbeit selbstständig verfasst zu haben. Ich habe keine anderen Quellen und Hilfsmittel als die angegebenen verwendet.

Ort, Datum	Michael Bertsch

Abstract

The application of impedance boundary conditions reduces the computational cost of CFD (computational fluid dynamics) simulations. For example, if one is only interested in combustion stability, it is possible to simulate the combustion chamber only. The remaining parts of the engine up- and downstream of the combustion chamber are modelled by impedance boundary conditions. The aim of this thesis is to evaluate the impedance boundary conditions implemented in ANSYS Fluent. Therefore we investigate the non-reflecting outlet of laminar and turbulent pipe flows. In another setup the influence of non-reflecting wall sections is examined for laminar and turbulent pipe flows. In addition, we prescribe an impedance at the inlet and outlet of laminar and turbulent pipe flows. Finally, we evaluate non-reflecting walls in combustion chambers.

Using impedance boundary conditions at inlets or outlets, one can model orifices. Setting the reflection coefficient for acoustic waves by means of imposing an impedance on an in- or outflow boundary is practicable in principle. However, when measuring the flow variables on this boundary, thus determining the actual reflection coefficient, observed and imposed reflection coefficient diverge. In contrast to the imposed reflection coefficient, the boundary shows reflecting behaviour towards low frequencies. This behaviour is observed for laminar and turbulent test cases. The reason is an additional constraint to prevent the mean fields from drifting. Non-reflecting behaviour at low frequencies improves when the characteristic domain length is larger.

Another part of this thesis is dedicated to the evaluation of the consequences when imposing a non-reflecting boundary condition on the walls of the domain, which can be used to model mufflers. When changing the behaviour of a wall section from reflecting to non-reflecting, the magnitude of downstream propagating acoustic waves decreases considerably.

Sequential combustors are prone to transverse thermal instabilities, which can be eliminated in a simulation using non-reflecting walls. Therefore we investigate the influence of non-reflecting walls on a stable combustion simulation. Two combustion test cases are used to determine the influence of the acoustic parameters of the combustion chamber wall on the flame. It shows that setting the combustion chamber walls to non-reflecting has only a marginal effect on mean flow fields. The flame position does not change when using non-reflecting walls.

Contents

Nomenclature

Roman Symbols

$\hat{R}$	complex reflection coefficient	[1]
$\mathscr{L}_i$	characteristic wave amplitude	[m/s]
c	speed of sound	[m/s]
c_p	specific heat capacity at constant pressure	[J/(kg K)]
CFL	Courant-Friedrich-Lewy number	[1]
f	frequency	[Hz]
$f(s)$	characteristic wave - downstream propagating	[m/s]
$g(s)$	characteristic wave - upstream propagating	[m/s]
M	Mach number	[1]
M_w	relative molecular weight	[1]
p	total pressure	[Pa]
p_{abs}	absolute pressure	[Pa]
p_{gauge}	gauge pressure	[Pa]
p_{op}	operating pressure	[Pa]
R	reflection coefficient	[1]
R_{univ}	universal gas constant	[J/(mol K)]
s	specific entropy	[J/(kg K)]
T	temperature	[K]
u	flow speed	[m/s]

Greek Symbols

γ	ratio of specific heat capacities	[1]
λ	thermal conductivity	[W/(m K)]
λ_i	characteristic speed	[m/s]
Ψ_i	characteristic variable	[depends]
ρ	density	[kg/m^3]
$\underline{\underline{\sigma}}$	Cauchy stress tensor	[Pa]

Acronyms

ARX	autoregressive with exogenous input
BC	boundary condition
BJ	Box-Jenkins
CBSBC	characteristic based state-space boundary condition
CFD	computational fluid dynamics
CFL	Courant–Friedrichs–Lewy
FIR	finite impulse response
LES	large eddy simulation
NSCBC	Navier-Stokes characteristic boundary conditions
OE	output-error
PDE	partial differential equation
TDABC	time-domain admittance boundary condition
TDIBC	time domain impedance boundary condition
UDF	user defined function
WALE	wall-adapting local-eddy-viscosity

1 Introduction

1.1 Objectives

Impedance boundary conditions are of great importance for the investigation of thermoacoustic systems. In many cases, they allow for a reduction of the simulation domain. For example, instead of simulating an entire engine, impedance boundary conditions allow for performing a LES of the combustion chamber only. The parts which are not included in the CFD simulation are modelled by impedance boundary conditions. Thus significantly reducing the computational costs of the simulation and simplifying the design of the combustion chamber, without however neglecting the acoustic behaviour of the rest of the system. Impedance boundary conditions are implemented in ANSYS Fluent by convolution in the time domain. Fig. 1.1 schematically shows a turbomachine and the simplified model of the combustion chamber, in which the influence of the other components on thermoacoustic phenomena is modelled by means of an appropriate acoustic impedance.

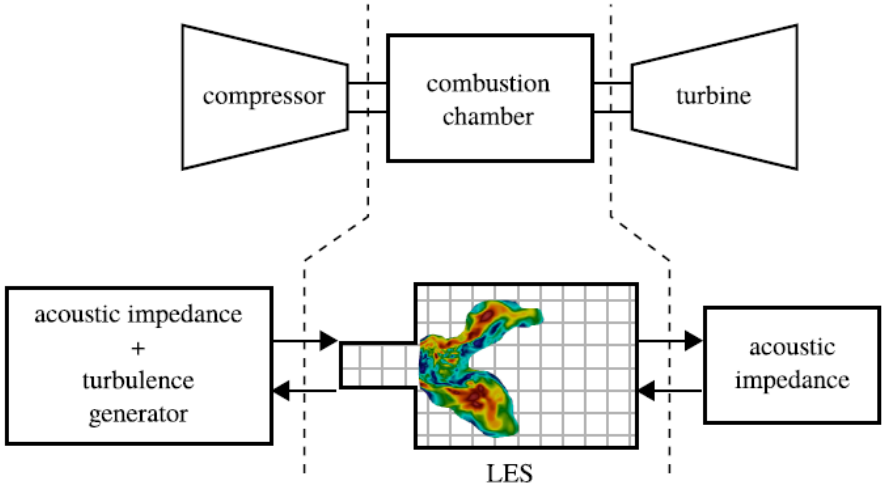

Figure 1.1: Schematic representation of the set-up of a LES of a combustion chamber while modelling the other parts of the system by means of impedance boundary conditions. Reprinted from Jaensch et al. [10].

This thesis aims to evaluate the built-in impedance boundary conditions in ANSYS Fluent in laminar and turbulent flow conditions. Acoustic impedance is applied on the inlet and the outlet of the chamber. The influence of a non-reflecting wall patch is investigated for non-reacting laminar and turbulent flow conditions in a duct and for a turbulent swirl burner.

1.2 Outline

The theoretical principles of computational fluid dynamics are summarized in Sec. 2.1. This includes the governing equations as well as an introduction to numerical methods. On this basis, Sec. 2.2 introduces the basic principles of thermoacoustics, focussing on the principle of acoustic waves. This section introduces the essential aspect of defining an acoustic reflection coefficient on a boundary. Therefore the concept of non-reflecting boundary conditions is presented in Sec. 2.3. Based on this, the impedance boundary condition is introduced in Sec. 2.4, whereas Sec. 2.5 gives an overview over the relevant theory of system identification, which is used to identify the impedance.

In order to better understand the obtained simulation results, Sec. 3 gives an insight into the algorithms and approaches typical for this finite-volume solver.

The various test cases used for the validation of the impedance boundary conditions are presented in Sec. 4. This includes a description of the setups of laminar and turbulent test cases and also discusses the results of the simulations and evaluates the possibilities of implementing impedance boundary conditions in ANSYS Fluent with regards to the findings of preceding studies on this subject. This section is divided into five subsections: At first, the reflecting behaviour of outflow boundaries specified as non-reflecting is presented for laminar and turbulent flow conditions in Sec 4.1. The implementation of wall impedance is described in Sec. 4.2. The investigation of the impedance boundary condition is treated in Sec. 4.3, followed by the examination of the combustion test cases in Sec. 4.4. In addition, Sec. 4.4.3 summarises the examination of the reflecting behaviour of a combustion chamber wall set to non-reflecting behaviour when applying a transverse excitation signal on the opposite wall in presence of a combustion process. The overall conclusion as well as a perspective for further studies in this area is given in Sec. 5.

2 Theoretical principles

2.1 Computational fluid dynamics

2.1.1 Navier-Stokes equations

The Navier-Stokes equations are the foundation of the mathematical description of a fluid-dynamics and heat-transfer problem. They are a system of partial differential equations (PDE) [18]. As this thesis aims at investigating acoustic phenomena, a compressible solver is chosen. The basic equations solved by ANSYS Fluent for compressible flows are the continuity, momentum, energy and, eventually, a species transport equation. The first PDE is the continuity equation

$$\frac{\partial \rho}{\partial t} + \nabla \cdot (\rho \vec{u}) = S_m, \tag{2.1}$$

where ρ denotes the density of the fluid, $\vec{u}$ is the velocity vector and S_m is a mass source term. Another PDE which is part of the Navier-Stokes equations is the momentum conservation equation, here in its differential form

$$\frac{\partial (\rho \vec{u})}{\partial t} + \nabla \cdot ((\rho \vec{u}) \otimes \vec{u}) = -\nabla p + \rho \vec{g} + \vec{F}, \tag{2.2}$$

where $\rho \vec{g}$ is the gravitational body force and $\vec{F}$ designates external body forces. For each chemical species, the species transport equation

$$\frac{\partial}{\partial t}\left(\rho Y_i\right) + \nabla \cdot \left(\rho \vec{u} Y_i\right) = -\nabla \cdot \vec{J}_i + R_i + S_i \tag{2.3}$$

is solved. Where Y_i designates the local mass fraction of species i, $\vec{J}_i$ is the diffusion flux of each species as a result of concentration and temperature gradients. R_i describes the net rate of production by chemical reaction and S_i designates the rate of creation of species i from a dispersed phase. The energy conservation equation in differential form

$$\frac{\partial}{\partial t}\left(\rho E\right) + \nabla \cdot \left(\vec{u}\left(\rho E + p\right)\right) = -\nabla \cdot \left(\sum_j h_j J_j\right) + S_h \tag{2.4}$$

completes the set of PDE which constitute the Navier-Stokes equations which ANSYS Fluent solves for compressible flow problems. E denotes the total energy, h_J is the enthalpy of each species, J_j is the mass flux of each species and S_h denotes an energy source term [1].

2.1.2 Numerical methods

The Courant–Friedrichs–Lewy (CFL) condition is represented for the one-dimensional case by

$$CFL = \frac{u \cdot \triangle t}{\triangle x} \leq C_{max}. \tag{2.5}$$

Where CFL denotes the CFL number, u is the velocity amplitude, $\triangle t$ is the discrete time step size and $\triangle x$ is the space increment. The maximum CFL number C_{max} with which a converged solution can be achieved, depends on the solver type and the simulation setup.

2.2 Acoustics

As this thesis examines the behaviour of acoustic waves in a straight and cylindrical pipe, the theoretical principles of acoustics shall be briefly summarized in this chapter. The foundation for describing a transport process is the scalar conservation law

$$\frac{\partial \phi}{\partial t} + \nabla \cdot F(\phi) = 0 \tag{2.6}$$

for a scalar $\phi(x,t)$. $F(\phi)$ denotes a scalar field of the variable ϕ. In integral form, this equation yields

$$\int_V \frac{\partial \phi}{\partial t} \mathrm{d}V + \int_V \nabla \cdot F(\phi) \, \mathrm{d}V = 0. \tag{2.7}$$

Which can be transformed to

$$\int_V \frac{\partial \phi}{\partial t} \mathrm{d}V = - \oint_S F(\phi) \cdot \vec{n} \, \mathrm{d}S \tag{2.8}$$

applying the Gaussian theorem on the second term of Eq. (2.7). This equation represents the conservation law on the level of control volumes. Restricting the observation to one dimension, the ∇ operator in Eq. (2.6) can be substituted with a space derivative, which yields

$$\frac{\partial \phi}{\partial t} + \frac{\partial F(\phi)}{\partial x} = 0. \tag{2.9}$$

Applying the chain rule of calculus leads to the equation

$$\frac{\partial \phi}{\partial t} + \frac{\partial F(\phi)}{\partial \phi} \cdot \frac{\partial \phi}{\partial x} = 0, \tag{2.10}$$

which allows for drawing a conclusion by dimensional analysis: ϕ is a dimensionless value, therefore the time derivative is in $\frac{1}{s}$ and the derivative in space is in $\frac{1}{m}$. As a result, the unit of the expression $\frac{\partial F(\phi)}{\partial \phi}$ is $\frac{m}{s}$ and thus a speed [17]. This term being of importance for the propagation of acoustic waves is defined as

$$\lambda(\phi) := \frac{\partial F(\phi)}{\partial \phi}. \tag{2.11}$$

As a first step to understand the physical meaning of $\lambda(\phi)$, the total differential of $\phi(x,t)$ in one dimension is determined to

$$\mathrm{d}\phi = \frac{\partial \phi}{\partial x} \cdot \mathrm{d}x + \frac{\partial \phi}{\partial t} \cdot \mathrm{d}t. \tag{2.12}$$

Inserting Eq. (2.12) in (2.10) and (2.11) yields

$$\mathrm{d}\phi = \frac{\partial \phi}{\partial x} \left(\mathrm{d}x - \lambda(\phi) \cdot \mathrm{d}t \right), \tag{2.13}$$

which leads to the conclusion that $d\phi$ is zero, if

$$\frac{\mathrm{d}x}{\mathrm{d}t} = \lambda(\phi). \tag{2.14}$$

Which implies that $\phi(x,t)$ is constant. In conclusion, if a scalar variable $\phi(x,t)$, which satisfies a differential equation as in (2.10), is constant along a curve $x(t)$, then this curve is referred to as a characteristic curve and $\lambda(\phi)$ as characteristic transport velocity [17].

2.2.1 Characteristic variables

For a transient, one-dimensional flow problem the Euler equations can be expressed as

$$\begin{aligned} \frac{\partial \rho}{\partial t} + u \cdot \frac{\partial \rho}{\partial x} + \rho \cdot \frac{\partial u}{\partial x} &= 0, \\ \frac{\partial u}{\partial t} + u \cdot \frac{\partial u}{\partial x} + \frac{1}{\rho} \cdot \frac{\partial p}{\partial x} &= 0, \\ \frac{\partial s}{\partial t} + u \cdot \frac{\partial s}{\partial x} &= 0, \end{aligned} \tag{2.15}$$

whereas s denotes the specific entropy of the control volume. Using isotropy and the definition of the speed of sound

$$c^2 := \left. \frac{\partial p}{\partial \rho} \right|_{s=const.} \tag{2.16}$$

allows for transforming the derivatives of pressure in the Euler equations and leads to

$$\begin{aligned} \frac{\partial \rho}{\partial t} + u \cdot \frac{\partial \rho}{\partial x} + \rho \cdot \frac{\partial u}{\partial x} &= 0, \\ \frac{\partial u}{\partial t} + u \cdot \frac{\partial u}{\partial x} + \frac{c^2}{\rho} \cdot \frac{\partial \rho}{\partial x} &= 0, \\ \frac{\partial s}{\partial t} + u \cdot \frac{\partial s}{\partial x} &= 0. \end{aligned} \tag{2.17}$$

This system of equations can be expressed in matrix format in quasi-linear form

$$\frac{\partial}{\partial t}\begin{pmatrix}\rho\\u\\s\end{pmatrix}+\begin{pmatrix}u & \rho & 0\\ \frac{c^2}{\rho} & u & 0\\ 0 & 0 & u\end{pmatrix}\cdot\frac{\partial}{\partial x}\begin{pmatrix}\rho\\u\\s\end{pmatrix}=\begin{pmatrix}0\\0\\0\end{pmatrix}, \tag{2.18}$$

or in symbolic form

$$\frac{\partial\vec{\phi}}{\partial t}+\underline{\underline{A}}(\vec{\phi})\cdot\frac{\partial\vec{\phi}}{\partial x}=\vec{0}, \tag{2.19}$$

whereas $\vec{\phi}$ denotes the state vector. In the next step, the eigenvalues of $\underline{\underline{A}}$ are determined to

$$\begin{aligned}\lambda_1 &= u-c,\\ \lambda_2 &= u+c,\\ \lambda_3 &= u.\end{aligned} \tag{2.20}$$

Then the matrix of the corresponding eigenvectors $\underline{\underline{R}}$ and its inverse matrix $\underline{\underline{R}}^{-1}$ can be calculated as

$$\underline{\underline{R}}=\begin{pmatrix}1 & 1 & 0\\ -\frac{\rho}{c} & \frac{\rho}{c} & 0\\ 0 & 0 & 1\end{pmatrix} \tag{2.21}$$

and

$$\underline{\underline{R}}^{-1}=\frac{1}{2}\begin{pmatrix}1 & -\frac{\rho}{c} & 0\\ 1 & \frac{\rho}{c} & 0\\ 0 & 0 & 2\end{pmatrix}. \tag{2.22}$$

The derivative in time of the characteristic variables Ψ_1,Ψ_2 and Ψ_3 is defined as the vector product of the inverse of the eigenmatrix and the state vector

$$\underline{\underline{R}}^{-1}\cdot\frac{\partial}{\partial t}\begin{pmatrix}\rho\\u\\s\end{pmatrix}=\frac{1}{2}\begin{pmatrix}\frac{\partial}{\partial t}\rho-\frac{\rho}{c}\frac{\partial}{\partial t}u\\ \frac{\partial}{\partial t}\rho+\frac{\rho}{c}\frac{\partial}{\partial t}u\\ 2\frac{\partial}{\partial t}s\end{pmatrix}=:\frac{\partial}{\partial t}\begin{pmatrix}\Psi_1\\\Psi_2\\\Psi_3\end{pmatrix}. \tag{2.23}$$

The results of these considerations in condensed form are expressed by the equation

$$\frac{\partial\vec{\Psi}}{\partial t}+\begin{pmatrix}\lambda_1 & 0 & 0\\ 0 & \lambda_2 & 0\\ 0 & 0 & \lambda_3\end{pmatrix}\cdot\frac{\partial\vec{\Psi}}{\partial x}=\vec{0}, \tag{2.24}$$

which relates the characteristic variables and corresponding characteristic propagation speed [17].

2.2.2 Characterisitc wave propagation

The general approach of describing acoustic waves presented in Sec. 2.2.1 can be expanded to laminar or turbulent flows with transient flow velocity. The flow fields of pressure $p(\vec{x},t)$, velocity $u(\vec{x},t)$ and density $\rho(\vec{x},t)$ can be separated into mean value $\overline{(.)}$ and acoustic fluctuation $(.)'$. In the case of a turbulent flow, there is turbulent fluctuation $(.)'_t$ as a third component. For the linear one-dimensional case there is an analytical solution for the state of the fluctuation of the flow fields as a function of time and space

$$\begin{aligned} p'(x,t) &= \overline{\rho c}\left(f(x,t)+g(x,t)\right) \\ u'(x,t) &= f(x,t)-g(x,t), \end{aligned} \tag{2.25}$$

where the f wave propagates with $\overline{u}+\overline{c}$ and the g wave propagates with $\overline{u}-\overline{c}$. f is the amplitude of a downstream propagating wave and g is the amplitude of an upstream propagating acoustic wave. Analogously, the characteristic wave amplitudes f and g can be expressed as a function of u' and p' [21]

$$\begin{aligned} f(x,t) &= \frac{1}{2}\left(\frac{p'(x,t)}{\overline{\rho}\,\overline{c}}+u'(x,t)\right) \\ g(x,t) &= \frac{1}{2}\left(\frac{p'(x,t)}{\overline{\rho}\,\overline{c}}-u'(x,t)\right). \end{aligned} \tag{2.26}$$

The ratio of reflection and transmission of the wave depends on the imposed boundary conditions on the interface. Amplitude and phase of the reflected or transmitted wave differ from the parameters of the incoming wave. Fig. 2.1 schematically shows the propagation behaviour of acoustic waves.

Figure 2.1: Schematic representation of acoustic waves entering and leaving a domain at the in- and outflow boundary. Adapted from Sovardi et al. [20].

The impedance boundary conditions define amplitude and phase of the waves f_u and g_d, which are entering the domain. The f_d wave, having propagated through the domain, arrives at the outlet interface and is partially transmitted and partially reflected, so is the g_u wave at the inlet boundary.

Another notation for the acoustic fields is the harmonic wave form

$$\begin{aligned} p'(x,t) &= \mathrm{Re}\left(\hat{p}(x)e^{i\omega t}\right) \\ u'(x,t) &= \mathrm{Re}\left(\hat{u}(x)e^{i\omega t}\right) \\ \rho'(x,t) &= \mathrm{Re}\left(\hat{\rho}(x)e^{i\omega t}\right), \end{aligned} \tag{2.27}$$

whereas ω denotes the angular frequency and Re(.) indicates the real part of a complex number. With these expressions, a reflection coefficient $\hat{R}$ can be defined at the outflow and inflow boundary following Tudisco et al. [22], using the ratio of reflected and incoming wave in the frequency domain

$$\begin{aligned} \hat{R}_{outflow} &= \frac{\hat{g}_u^B}{\hat{f}_u^B} \\ \hat{R}_{inflow} &= \frac{\hat{f}_d^A}{\hat{g}_d^A}. \end{aligned} \tag{2.28}$$

The description of characteristic waves presented in Sec. 2.2.1 can be extended to three dimensions. The characteristic wave amplitudes $\mathscr{L}_i$ and their characteristic speeds λ_i are schematically represented in Fig. 2.2 for a three-dimensional domain.

The characteristic wave amplitudes can be expressed as functions of the primitive variables p, u and ρ

$$\begin{aligned} \mathscr{L}_1 &= \lambda_1\left(\frac{\partial p}{\partial x_1} - \rho c\frac{\partial u_1}{\partial x_1}\right) \\ \mathscr{L}_2 &= \lambda_2\left(c^2\frac{\partial \rho}{\partial x_1} - \frac{\partial p}{\partial x_1}\right) \\ \mathscr{L}_3 &= \lambda_3\left(\frac{\partial u_2}{\partial x_1}\right) \\ \mathscr{L}_4 &= \lambda_4\left(\frac{\partial u_3}{\partial x_1}\right) \\ \mathscr{L}_5 &= \lambda_5\left(\frac{\partial p}{\partial x_1} + \rho c\frac{\partial u_1}{\partial x_1}\right). \end{aligned} \tag{2.29}$$

The corresponding characteristic speeds are

$$\begin{aligned} \lambda_1 &= u_1 - c \\ \lambda_2 = \lambda_3 = \lambda_4 &= u_1 \\ \lambda_5 &= u_1 + c \end{aligned} \tag{2.30}$$

as derived for the one-dimensional case. The characteristic wave amplitudes f and g, as defined in Eq. (2.26), are per definition constant along the characteristic curves $x + \lambda_i t = const.$, which is why they are referred to as Riemann-invariants [22].

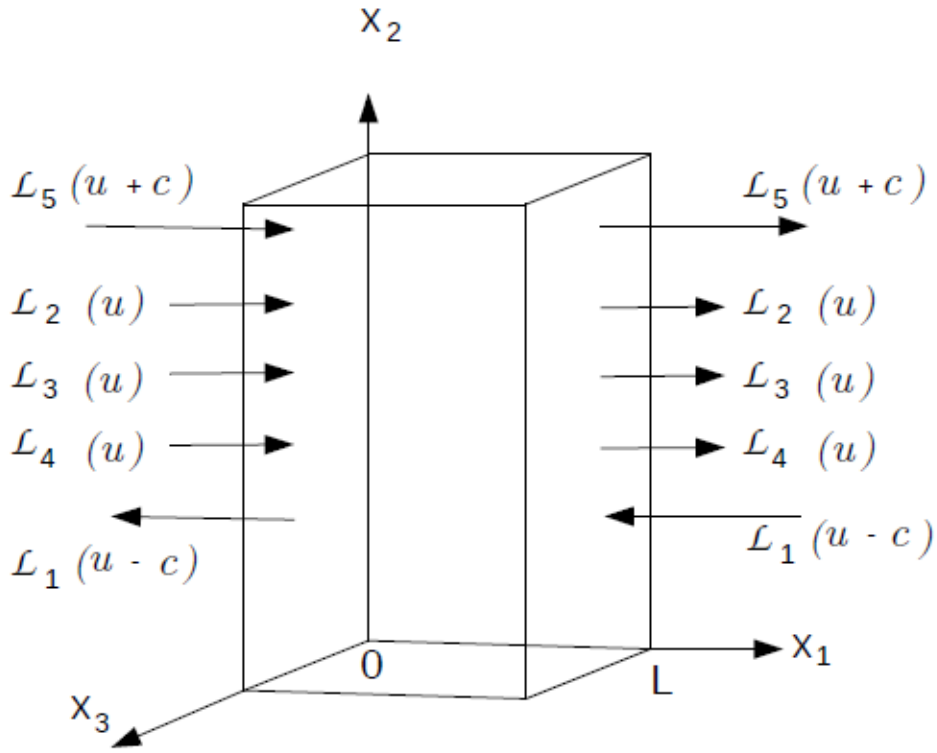

Figure 2.2: Schematic three-dimensional representation of the direction, amplitude and speed of characteristic waves entering (left) and leaving (right) the domain. Reprinted from Tudisco et al. [22].

In case of a simulation, the characteristic waves presented in this section are set according to a certain boundary condition type. This procedure is described in detail in the following section.

2.3 Reflecting behaviour of an outflow boundary

The reflecting behaviour of a boundary depends on the type of the imposed boundary condition. For instance, we consider the x_2x_3 outflow boundary at $x_1 = L$ in Fig. 2.2. For an upstream propagating acoustic wave g inside the domain at the considered boundary face, the Riemann invariance can be expressed as

$$\frac{\partial g}{\partial t} + \bar{\lambda}_1 \frac{\partial g}{\partial x_1} = 0. \tag{2.31}$$

This equation can be reformulated using the definition of the acoustic g wave in Eq. (2.26) and the expression for the fluctuation of the characteristic wave $\mathscr{L}_1$ in (2.29) into

$$\frac{\partial g}{\partial t} + \lambda_1 \frac{\partial g}{\partial x_1} = \frac{\partial g}{\partial t} + \frac{\lambda_1}{2}\left(\frac{1}{\bar{\rho}\bar{c}}\frac{\partial p'}{\partial x_1} - \frac{\partial u'}{\partial x_1}\right) = \frac{\partial g}{\partial t} + \frac{\mathscr{L}_1'}{2\bar{\rho}\bar{c}} = 0. \tag{2.32}$$

This expression can in turn be reformulated into

$$\mathscr{L}_1' = -2\bar{\rho}\bar{c}\frac{\partial g}{\partial t}. \tag{2.33}$$

This expression shows the direct correlation between the upstream propagating acoustic wave g and the characteristic wave fluctuation $\mathscr{L}_1'$ on the outlet boundary. With the assumption of harmonic waves

$$g(x,t) = \mathrm{Re}\left(\hat{g}e^{i\omega t}\right), \tag{2.34}$$

where $\hat{g}$ denotes the amplitude of the characteristic wave in the frequency domain and ω is the angular frequency, Eq. (2.33) can be expressed as

$$\mathscr{L}_1' = -2i\bar{\rho}\bar{c}\omega\hat{g}e^{i\omega t}. \tag{2.35}$$

This demonstrates, that the amplitude of the upstream propagating acoustic wave g on the boundary depends directly on the imposed characteristic wave fluctuation $\mathscr{L}_1'$ [22].

2.3.1 Restrictions for non-reflecting boundary conditions

As a result, it is not possible to impose the mean flow quantities and to specify the characteristic wave signal at the boundary at the same time. This restriction is described by Tudisco et al. [22]. If a perfectly non-reflecting boundary condition is imposed, then the mean flow quantities might drift as described by Poinsot et al. [8]. A trade-off between the mean flow and impedance boundary conditions is needed. A linear relaxation coefficient K can be used to calculate the characteristic wave $\mathscr{L}_1$ on the outlet. In the following, the concept of using a relaxation factor is introduced for an outflow boundary, where the mean pressure is imposed. Depending on the value of the relaxation coefficient, a correction term changes the pressure value towards the constant target pressure p_∞ imposed on the boundary. This algorithm is explained in Sec. 3.2. The upstream propagating characteristic wave is defined as

$$\mathscr{L}_1 = -K\left(p - p_\infty\right), \tag{2.36}$$

where the term $\left(p - p_\infty\right)$ describes the imposed pressure fluctuation on the boundary. Applying the relation between acoustic pressure fluctuation and acoustic waves given in Eq. (2.25) after Fourier transform, the characteristic wave can be expressed in the frequency domain as

$$\hat{\mathscr{L}}_1 = \bar{\rho}\bar{c}K\left(\hat{f} + \hat{g}\right)e^{i\omega t}. \tag{2.37}$$

This formulation is based on the assumption, that the pressure drift fluctuation $\left(p - p_\infty\right)'$ can be described by characteristic linearised waves. Equating the expression with Eq. (2.35) leads to

$$-2i\bar{\rho}\bar{c}\omega\hat{g} = \bar{\rho}\bar{c}K\left(\hat{f}+\hat{g}\right). \tag{2.38}$$

Neglecting external excitation, the reflection coefficient on the outlet boundary can thus be expressed as

$$\hat{R} = \frac{\hat{g}}{\hat{f}} = \frac{-1}{\frac{2i\omega}{K}+1}. \tag{2.39}$$

Therefore, the reflection coefficient $\hat{R}$ is -1 for $K \neq 0$ and $\omega \to 0$, that is, the behaviour is reflecting for acoustic waves at low frequencies. A completely reflecting boundary can also be characterized by $K \to \infty$. This corresponds to a reflection coefficient $\hat{R}$ of -1 with an amplitude of 1 and a phase value of 180°, whereas $K \to 0$ describes ideal non-reflecting acoustic behaviour. But, as a relaxation coefficient of $K = 0$ does not prevent drift of the flow quantities, this ideal behaviour cannot be achieved. Thus making it necessary to find a compromise between imposing the desired acoustic behaviour and the correct mean field quantities on the boundary [22].

This restriction regarding the concurrent specification of mean flow and reflecting behaviour, is of great importance when investigating impedance boundary conditions.

2.4 Impedance boundary conditions

By imposing an impedance boundary condition, the acoustic reflection coefficient of a boundary can be specified according to the requirements. Typically, the reflection coefficient is frequency-dependend. There are different methods of imposing impedance boundary conditions. Either the acoustic impedance, or the reflection coefficient is imposed on the boundary. In both cases, the expressions have to be transformed to the time domain. The transformation from the frequency domain can be achieved by convolution integral of acoustic quantities and reflection coefficient. The other method of modelling an impedance boundary condition is the state space approach using CBSBC (characterisic based state-space boundary conditions) [10].

In Fluent, impedance boundary conditions are implemented by means of a convolution integral. For a description of the convolution method, the reader is referred to Sec. 3.3. We use the convolution integral mehtod because it is implemented in Fluent.

2.5 System identification

A simple way to compute the relation between the acoustic waves anywhere in the computational domain is single frequency excitation. This has the drawback that a separate simulation is necessary for each frequency at which the relation of two acoustic waves is of interest. Broadband excitation is faster, as it allows to determine the response for a broad frequency range in one simulation. When using this approach, a linear time invariant (LTI) system is fitted using the resulting broadband signals.

A set of models is necessary to identify the transfer functions between characteristic wave amplitudes at different positions or of different waves. For this identification process, the choice of a suitable single-input single-output model is essential. The system is assumed to be linear. In this case, input-output models give reliable results. In thermoacoustics, commonly used models are FIR (finite impulse response) [15], ARX (autoregressive with exogenious input) [7], OE (output-error) [7] and BJ (Box-Jenkins) [19]. FIR is commonly used for the identification of the flame transfer function, whereas ARX, OE and BJ are typically used to identify scattering matrices and reflection coefficients. In this evaluation we use the OE models to identify the reflection coefficient.

The FIR (finite impulse response) is the simplest model of the above mentioned. The output y is modelled based on the input u. The relation between input and output is

$$y(t) = b_1 u(t-1) + ... + b_m u(t-m) + e(t), \tag{2.40}$$

where $e(t)$ is unknown white noise and m is the number of coefficients. The advantage of this model is, that it is always stable. However, noise is fitted, which might cause oscillations.

In case of the ARX model (autoregressive with exogenous input), the relation between input u and output y in the time domain is given by the equation

$$y(t) + a_1 y(t-1) + ... + a_{n_a} y(t-n_a) = b_1 u(t-n_k) + ... + b_{n_b} u(t-n_b-n_k+1) + e(t), \tag{2.41}$$

whereas $e(t)$ designates the error in form of white noise, n_a is the number of poles, n_b is the number of zeros of the model and n_k describes the time delay. In matrix form, the ARX model can be expressed as

$$Ay(t) = Bu(t-n_k) + e(t). \tag{2.42}$$

In some cases, the disadvantage of this model type is, that the modelling of the error depends on the input, namely $\frac{1}{A}$ compared to $\frac{B}{A}$ for the input, this is, the poles for system dynamics and the error model are the same. Fig. 2.3 gives a schematic overview of the ARX model, as well as of the output-error (OE) and Box-Jenkins (BJ) model.

The OE model is similar to the ARX model. The matrix formulation is

$$y(t) = \frac{B}{F} u(t-n_k) + e(t), \tag{2.43}$$

which shows, that the model only takes into account inputs. Furthermore, the description of noise is neglected. The focus of this model type is the minimization of prediction error. The BJ model is an extension of the ARX model, as input and input error are treated independently. The model can be described in matrix form as

$$y(t) = \frac{B}{F} u(t-n_k) + \frac{C}{D} e(t). \tag{2.44}$$

This model is very flexible and still gives good results when measurement noise is relatively large [12], [13].

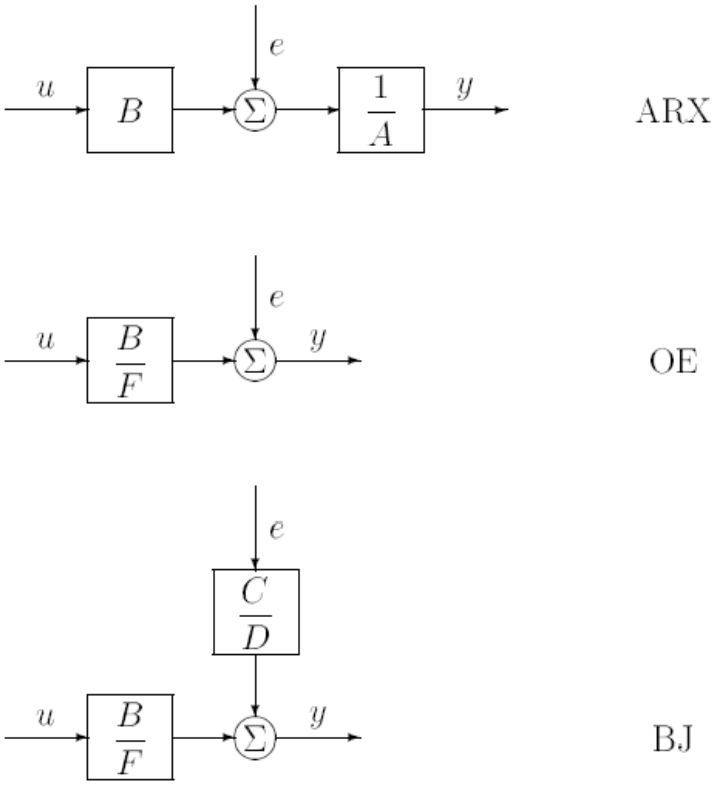

Figure 2.3: Schematic representation of the linear input-output models ARX, OE and BJ. Each with respective transfer functions. Adapted and reprinted from Ljung [12].

The accuracy of the thus estimated model can be defined in multiple ways. In this thesis, accuracy is defined based on the weighted difference between the output of the model and the measured output. For $y - \bar{y} \neq 0$, the accuracy value in percent $a_{\%}$ is calculated in the time domain as

$$a_{\%} = \left(1 - \frac{\|y - y^*\|}{\|y - \bar{y}\|}\right) \cdot 100\%, \tag{2.45}$$

where y designates the training set and y^* is the estimated output signal. $\bar{y}$ designates the mean value of the validation data output signal [13].

Single frequency excitation

Two different means of imposing an excitation signal are used to validate the test cases. The first approach consists of imposing a periodic signal of a certain constant frequency on the boundary. This signal can be the velocity fluctuation u' or the amplitude of an acoustic wave entering the domain. In the first laminar test case, the imposed signal is the flow velocity on the inlet, which oscillates around a mean value in form of a sinusoidal wave. The amplitude

of velocity- or f wave fluctuation is 5% of the mean flow speed for the laminar case and corresponds to a 5 or 20% fluctuation of the mean flow speed $\bar{u}$ for the turbulent test case. This results in a good signal to noise ratio, which is important especially with regard to the turbulent test case. The high computation cost restricts the number of simulations which can be performed. Thus limiting the amount of frequencies which for which the reflection coefficient can be determined using single frequency excitation. These limitations can be avoided by using a broadband excitation signal. However, single frequency excitation is used to validate the results of the simulations performed with broadband excitation, because it does not require any modelling.

The disadvantage of using single frequency excitation and identification is, that the confidence region is not computed. Only the averaged frequency response over some periods is calculated.

Broadband excitation

Broadband excitation allows for determining the thermoacoustic reflection behaviour of boundaries for a wide range of frequencies in a single simulation run, thus cutting the combined computational cost to a minimum. The challenge is to provide a high-quality broadband signal. The generated signals should have high power spectral density in the specified frequency range. We generate a signal bounded between -1 and 1, then we scale it appropriately to obtain 5% and 20% excitation of the velocity or incoming wave. Additionally, the high magnitude values should have the highest probability.

After generating the broadband fluctuation signal with maximum amplitudes of 1, oscillating around a mean value of 0, the signal is multiplied by factor of 5% and 20% of the mean value of the signal to be imposed on the boundary for laminar and turbulent test case, respectively. This fluctuation is then added to the mean value and saved in form of a time-velocity or time-wave amplitude profile. The generated signal is used as input for the inlet velocity or outlet f wave fluctuation.

Most often, we use broadband excitation for the investigation of the test cases. In addition, single frequency excitation for some frequencies is used to validate the identified model.

3 Flow simulation with ANSYS Fluent

3.1 Flow solvers

For all our investigations, we used ANSYS Fluent. In the following, we describe this finite volume solver. It offers a choice between two numerical methods: a pressure- and a density-based solver. While the former is mainly used for low-speed incompressible flows, the latter approach is used for high-speed compressible flows. For both methods, the calculation of the velocity field is based on the momentum equation, whereas the means of determining density and pressure fields differ: the pressure-based approach consists of extracting the pressure field by solving a pressure correction equation, which itself is derived from the continuity and momentum equations. In contrast to this, the density-based method uses the equation of state to obtain the pressure field and the continuity equation is the foundation for the calculation of the density field. Fluent solves the governing integral equations for the conservation of mass, momentum and energy as introduced in Sec. 2.1.1, and, if necessary, for turbulence and other scalar variables [2].

Dealing with pressure, Fluent uses the concept of operating pressure to minimise numerical round-off error. For a detailed explanation of this concept, the reader is referred to Appx. F. In the following, only the pressure-based solver is explained, as this solver is used for all simulations performed in the course of this thesis. Pressure-based solvers are more commonly used in the CFD community. Typically, they converge faster than density-based solvers.

Pressure-based solver

The pressure-based solver is based on an algorithm of the projection method. The conservation of mass in the velocity field is ensured by solving the pressure equation, which is derived from the continuity and momentum equation. Iterations are necessary in the solution process, because the governing equations are non-linear and coupled. The whole set of equations is solved iteratively for each time step until convergence is detected. There is a choice between a segregated and a coupled algorithm.

In the segregated algorithm the governing equations are solved separately one from another. Each equation is considered separately for each solution variable. This approach is memory-efficient, but convergence is slow for challenging cases compared to the coupled approach. Fig. 3.1 shows the algorithm for the segregated algorithm.

In the first step, the fluid properties are updated according to the current solution. Then all momentum equations are solved, using actual values of pressure and face mass flux. After that, the pressure correction equation is solved using the calculated velocity field. The

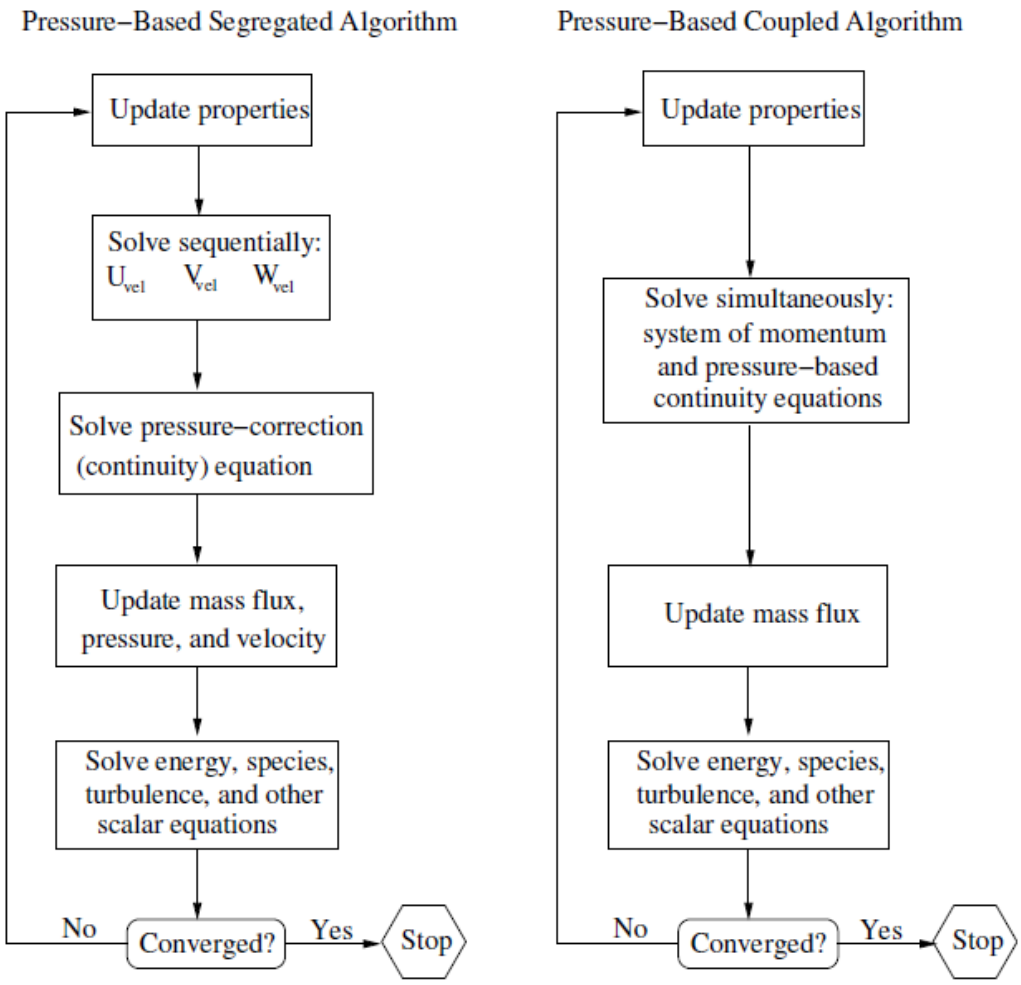

Figure 3.1: Schematic comparison of the algorithms of the segregated and the coupled algorithm of the pressure-based solver. Reprinted from the Fluent manual [2].

pressure correction is then used to correct face mass flux values, pressure and velocity field. Then, the equations for additional scalars such as energy, species and turbulent quantities are solved if the option is active. These steps are run through repetitively until convergence is reached.

In contrast, the coupled algorithm solver is based on a coupled system of momentum and continuity equations. The solution process is similar, except that the steps of solving the momentum and the pressure correction equation are combined. The other governing equations are solved in a segregated approach. The coupled algorithm improves solution convergence significantly. However, memory requirements rise accordingly and the computation time for one time step is longer [2].

3.2 Non-reflecting boundary conditions in Fluent

In Sec. 2.2.1 we introduced the concept of characteristic waves. In Fluent, non-reflecting boundary conditions are implemented using these characteristic waves, which are in turn calculated from the primitive flow variables pressure, temperature and x-, y- and z-velocity components. These flow quantities are obtained by solving the Euler equations on the boundary. Therefore, the Euler equations are transformed to a coordinate system with the x_1 axis being orthogonal to the boundary. A schematic representation of the coordinate transformation is shown in Fig. 3.2.

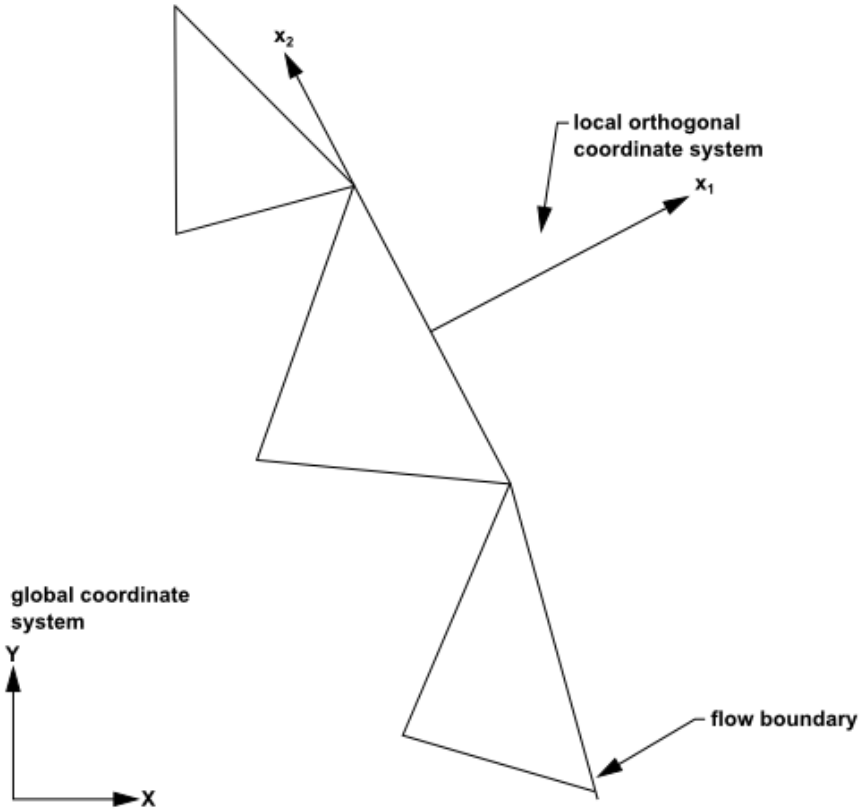

Figure 3.2: Schematic representation of global Cartesian (X,Y,Z) and local orthogonal (x_1, x_2, x_3) coordinate system on the boundary. Reprintend from the Fluent manual [3].

For certain boundary types, no information about the waves propagating into the computational domain from the outside is available. In this case, a special treatment of the Euler equations is necessary. Poinsot and Lele [8] derived a means of defining soft boundary conditions for non-reflecting boundary conditions. Therefore, on an non-reflecting boundary, in addition to the Navier-Stokes equations of the interior, a second system of equations is solved on the boundary:

$$
\begin{aligned}
&\frac{\partial \rho}{\partial t} + d_1 + \frac{\partial(\rho u_2)}{\partial x_2} + \frac{\partial(\rho u_3)}{\partial x_3} = 0 \\
&\frac{\partial(\rho u_1)}{\partial t} + u_1 d_1 + \rho d_3 + \frac{\partial(\rho u_1 u_2)}{\partial x_2} + \frac{\partial(\rho u_1 u_3)}{\partial x_3} = 0 \\
&\frac{(\partial \rho u_2)}{\partial t} + u_2 d_1 + \rho d_4 + \frac{\partial(\rho u_2^2)}{\partial x_2} + \frac{\partial(\rho u_2 u_3)}{\partial x_3} + \frac{\partial p}{\partial x_2} = 0 \\
&\frac{\partial(\rho u_3)}{\partial t} + u_3 d_1 + \rho d_5 + \frac{\partial(\rho u_3 u_2)}{\partial x_2} + \frac{\partial(\rho u_3^2)}{\partial x_3} + \frac{\partial p}{\partial x_3} = 0 \\
&\frac{\partial \rho E}{\partial t} + \frac{1}{2}|\vec{u}|^2 d_1 + \frac{d_2}{(\gamma-1)} + \rho u_1 d_3 + \rho u_2 d_4 + \rho u_3 d_5 + \frac{\partial(\rho E u_2 + p u_2)}{\partial x_2} + \frac{\partial(\rho E u_3 + p u_3)}{\partial x_3} = 0.
\end{aligned}
\tag{3.1}
$$

The velocity components u_i give the velocity in x_i direction of the local coordinate system, $\vec{u}$ designates the velocity vector in the same coordinate system and E is the total energy of the control volume. The d_i terms

$$
\begin{aligned}
d_1 &= \frac{1}{c^2}\left[\mathscr{L}_2 + \frac{1}{2}(\mathscr{L}_1 + \mathscr{L}_5)\right] \\
d_2 &= \frac{1}{c^2}(\mathscr{L}_1 + \mathscr{L}_5) \\
d_3 &= \frac{1}{2\rho c}(\mathscr{L}_5 - \mathscr{L}_1) \\
d_4 &= \mathscr{L}_3 \\
d_5 &= \mathscr{L}_4.
\end{aligned}
\tag{3.2}
$$

are calculated from the characteristic wave amplitudes $\mathscr{L}_i$ which were defined in Eq. (2.29) in Sec. 2.2.1.

Under subsonic flow conditions, four waves each are entering and leaving the domain on a boundary face. For an inflow boundary, the waves are entering the domain with the characteristic speeds $\lambda_1, \lambda_2, \lambda_3$ and λ_4 in negative x_1 direction. For an outflow boundary, the speeds corresponding to the outgoing acoustic waves are $\lambda_2, \lambda_3, \lambda_4$ and λ_5 in positive x_1 direction. The acoustic waves entering and leaving are shown in Fig. 3.3 for inflow and outflow boundary face respectively.

To implement a non-reflecting boundary condition at an inflow or outflow boundary condition, at first the flow derivatives parallel to the boundary from Eq. (3.1) are extrapolated from the interior of the domain using the relations from Eq. (3.2) to determine the amplitudes of waves leaving the domain. Then, incoming waves are determined by setting the characteristic waves $\mathscr{L}_3$ and $\mathscr{L}_4$ to zero. The linear relaxation method is used to determine the amplitudes of pressure and entropy wave entering the domain. This method is based on the assumption, that the amplitude of waves entering the computational domain is proportional to the relative

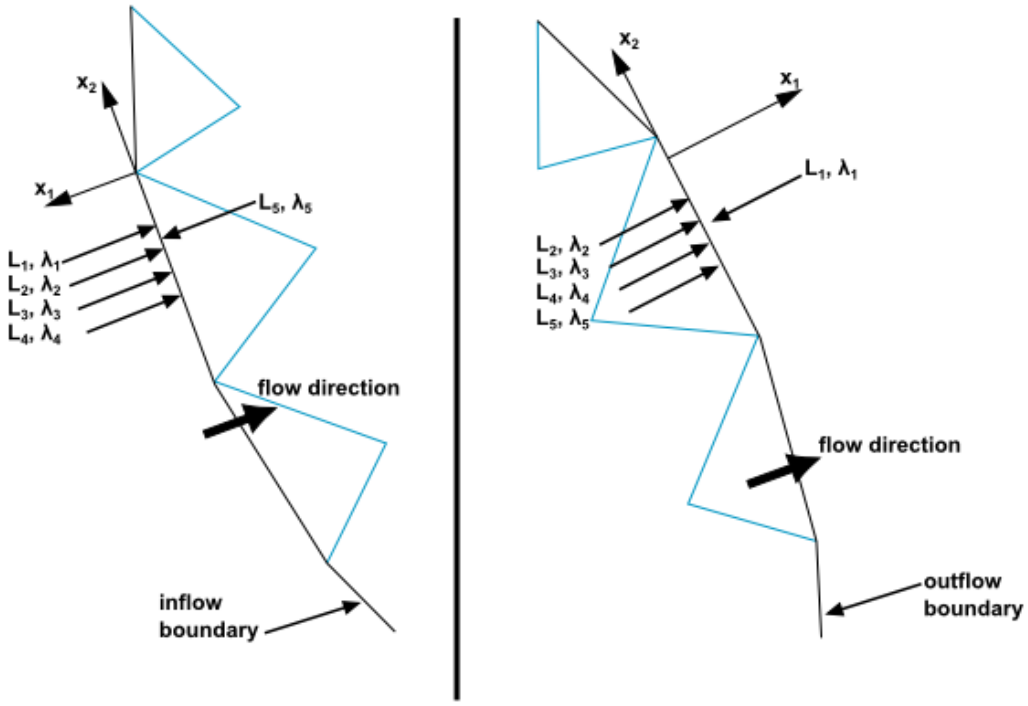

Figure 3.3: Schematic representation of characteristic waves entering (left) and leaving (right) the domain on a boundary with amplitudes $\mathscr{L}_i$ and characteristic speeds λ_i for subsonic flows. Reprintend from the Fluent manual [3].

distance between the local value of the primitive flow quantity and the value imposed on the boundary. The relation between imposed and local value is different for every type of in- or outflow boundary type. In this thesis, the examined in- and outflow boundaries are restricted to velocity inlets and pressure outlets. Therefore the expressions are only presented for these two boundary types.

For a pressure outlet, the incoming wave $\mathscr{L}_1$ is calculated as

$$\mathscr{L}_1 = K\left(p - p_{imposed}\right), \tag{3.3}$$

where $p_{imposed}$ denotes the imposed pressure value on the outflow boundary, p is the local pressure value in the boundary-adjacent cell, and K is a relaxation factor. As shown in Sec. 2.3.1, $K \rightarrow 0$ corresponds to ideal non-reflecting behaviour, whereas $K \rightarrow \infty$ corresponds to completely reflecting behaviour with zero offset.

Depending on this relaxation factor, the average pressure on the boundary can either be shifted towards a specified target value $p_{imposed}$ or relaxed towards the local pressure p. In the first case, the relaxation factor is calculated as

$$K = \sigma_2 c, \tag{3.4}$$

where the default value of σ_2 is 5.0. This is only possible when using the density-based solver. We do not consider the density-based solver in this investigation. In the second case, if the average pressure shall relax towards p on the boundary, the relaxation factor is

$$K = \sigma_1 \left(1 - M_{max}^2\right) \frac{c}{h}, \tag{3.5}$$

where σ_1 is an under-relaxation factor with a default value of 0.15, M_{max} denotes the maximum Mach number in the domain and h is the characteristic domain size, e.g. the length of a duct with axial flow. It is clear from Eq. (3.5), that the relaxation factor depends on the length of the domain. With increasing domain length, the relaxation factor becomes smaller and the behaviour of the boundary changes towards non-reflecting.

For a velocity inlet, the incoming waves $\mathscr{L}_1$ and $\mathscr{L}_2$ are calculated as

$$\begin{aligned} \mathscr{L}_1 &= -K\rho c \left(U_1 - U_{1,imposed}\right) \\ \mathscr{L}_2 &= Kc^2 \left(\rho - \rho_{derived}\right), \end{aligned} \tag{3.6}$$

where $U_{1,imposed}$ is the the velocity imposed on the boundary and $\rho_{derived}$ is the density on the boundary. The density is calculated using the imposed temperature on the boundary and the extrapolated pressure from the domain [3].

3.3 Impedance boundary conditions in Fluent

Fluent allows to impose an impedance boundary condition on inflow and outflow boundaries. The acoustic impedance $\hat{Z}$ is defined in the frequency domain as

$$\hat{Z}(\omega) = \frac{\hat{p}'}{\rho c \hat{u}'}, \tag{3.7}$$

where ω is the angular frequency, $\hat{p}'$ designates the acoustic pressure fluctuation in the frequency domain and $\hat{u}'$ is the velocity fluctuation in the frequency domain. However, Fluent being a time domain solver, the impedance has to be be transformed to the time domain. After the transformation, the relation between pressure and velocity fluctuation can be expressed in form of an integral as

$$p'(t) = \int_{-\infty}^{\infty} Z(\tau)\ u'(t-\tau)\ d\tau. \tag{3.8}$$

Fluent uses the concept of a reflection coefficient instead of impedance, which might be unbounded. For example, the impedance $Z \rightarrow \infty$ at a velocity inlet with zero velocity fluctuation. The reflection coefficient in the frequency domain can be expressed as a function of the acoustic impedance as

$$\hat{R}(\omega) = \frac{\hat{Z}(\omega) - 1}{\hat{Z}(\omega) + 1}, \tag{3.9}$$

which allows to rewrite Eq. (3.8) as

$$p'(t) - \rho c u'(t) = \int_{-\infty}^{\infty} R(\tau) \left(p'(t-\tau) + \rho c u'(t-\tau) \right) d\tau. \tag{3.10}$$

Fluent uses a discretised form of this convolution integral to link normal velocity fluctuation with the pressure fluctuation in the solving process. The determined acoustic fluctuations are added to the pressure and velocity computed from the equations for non-reflecting boundary conditions.

The impedance boundary condition has to be specified in the frequency domain with $s = j\omega$ in the form

$$\hat{R}(s) = D + \sum_{k=1}^{N_1} \frac{A_k}{(s+\lambda_k)} + \sum_{l=1}^{N_2} \left(\frac{B_l + iC_l}{(s+\alpha_l - i\beta_l)} + \frac{B_l - iC_l}{(s+\alpha_l + i\beta_l)} \right), \tag{3.11}$$

where D depicts a real term, N_1 and N_2 are the number of real and imaginary poles, λ_k depicts a real pole with the amplitude A_k. α_l and β_l constitute real and imaginary part of a complex conjugate pole with real and imaginary part of the amplitude B_l and C_l [4].

4 Test cases

4.1 Non-reflecting outflow boundary condition

In this section, the reflecting behaviour of outflow boundaries is examined under laminar and turbulent flow conditions. The aim is to determine to which extent boundaries set to non-reflecting show the prescribed behaviour by determining the acoustic reflection coefficient from monitored flow variables. It is essential to understand this behaviour as imposing a complex acoustic impedance on a boundary in ANSYS Fluent is based on non-reflecting behaviour which is then superimposed with the specified impedance.

4.1.1 Laminar pipe flow with non-reflecting outflow boundary

Setup

To evaluate the reflecting behaviour under laminar flow conditions, the setup of the laminar case from Jaensch et al. [10] is used. Their original mesh consisting of 40320 hexahedral cells is used for this investigation. The diameter of the duct is 30 mm and the length is 70 mm. The walls are modelled as standard slip-walls with a constant temperature of 300 K. The mean flow speed is 5 $\frac{m}{s}$ and a pressure of 101325 Pa is imposed at the outflow boundary. The outflow boundary is set to non-reflecting, whereas the inflow boundary is reflecting for acoustic waves. At the inflow boundary, an excitation signal in form of an inflow velocity fluctuation is applied. We are interested in frequencies from 0 to 5 kHz, therefore we use a broadband signal with corresponding frequencies. The monitored stream-wise velocity and static pressure data at the outflow boundary are used to calculate the down- and upstream propagating acoustic waves on this boundary. The outlet reflection coefficient is determined from the acoustic waves by means of system identification. Results from single frequency excitation are used to validate the identified system. Therefore sinusoidal mono-frequent excitation is used in additional simulation runs. The time step size is $2.5 \cdot 10^{-6}$ in order to limit the CFL number to 0.8. Simulation time is 0.05 s.

Results

The reflection coefficient determined by post-processing the monitored data is shown in Fig. 4.1. The post-processing steps are described in detail in Appx. C. The dashed line indicates the reflection coefficient as identified by means of system identification with an accuracy of 96% using an OE model. This is why the confidence regions, depicted as shaded regions in the plot, are relatively small. The confidence regions are given by $\pm 2.580\sigma$, which correspond to 99%

confidence for normal distribution with standard deviation σ. Results from single frequency validation runs are in good accordance with the identified reflection coefficient.

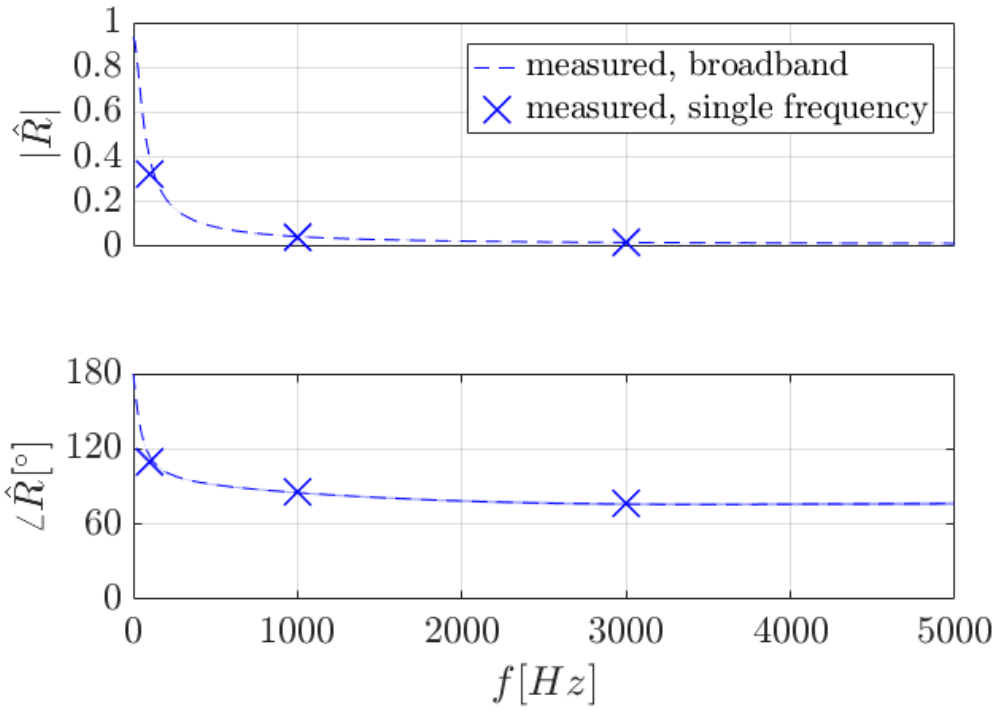

Figure 4.1: Reflection coefficient as determined at the centre of the outflow boundary for the laminar test case.

The amplitude of the reflection coefficient is below a value of 0.05 for frequencies between 500 and 5000 Hz. However, towards lower frequencies the amplitude of the reflection coefficient approaches a value of 1. Similar behaviour can be observed for the phase curve. The phase shift between incoming and outgoing acoustic wave at the outflow boundary is relatively steady at 75°, but approaches a value of 180° for frequencies approaching zero. Therefore the complex-valued reflection coefficient is -1 at $f = 0$ which corresponds to a standard pressure outlet. In conclusion, the behaviour at the outflow boundary is reflecting for low frequencies, whereas the specified non-reflecting behaviour can be observed to a limited extent above a certain frequency threshold. This problem was addressed in Sec. 2.3.1 and Sec. 3.2. For low frequencies, the non-reflecting boundary condition is reflecting to prevent mean value drift. Eq. (3.5) suggests that the non-reflecting behaviour could be improved for low frequencies by increasing the domain length. Such a study was indeed performed and can be seen in Appx. E.

4.1.2 Turbulent pipe flow with non-reflecting outflow boundary

Setup

The setup to examine impedance boundary conditions under turbulent flow conditions developed by Jaensch et al. [10] is used to test a non-reflecting boundary condition. Their mesh consisting of 517293 hexahedral cells was kindly provided. This number of cells ensures an adequate resolution for LES. As in the laminar case, a cylindrical duct with a diameter of 30 mm is used. The length is 150 mm for this setup. The walls are modelled as no-slip walls with a temperature of 300 K. The outflow boundary is modelled as a standard pressure outlet where the pressure is set to 101325 Pa. Non-reflecting behaviour is prescribed at the outflow boundary, whereas the inflow boundary is reflecting. The inflow boundary is modelled as a velocity inlet. The mean flow speed is 9 $\frac{m}{s}$. In addition, turbulence intensity is set to

$$\frac{\left(u'_{turb}\right)_{rms}}{\bar{u}} = \frac{1\frac{m}{s}}{9\frac{m}{s}} = 11.11\%, \tag{4.1}$$

where $\left(u'_{turb}\right)_{rms}$ is the root-mean-square value of the turbulent velocity fluctuations and $\bar{u}$ designates the mean flow speed. At the inflow boundary, an acoustic excitation signal is imposed in the form of a velocity fluctuation with a maximum amplitude of 20% of the mean flow speed. A broadband velocity signal with high power spectral density for frequencies up to 10 kHz is used. The reflection coefficient calculated from the broadband axial velocity and density signal at the outlet is validated by additional simulation runs with single frequency excitation signals. A time step size of $2.5 \cdot 10^{-6}$ results in a CFL number below 0.8. Simulation time is restricted to 0.1 s due to high computational cost.

Results

The reflection coefficient determined from the velocity and pressure data at the centre of the outflow boundary is shown in Fig. 4.3. The accuracy of the reflection coefficient determined by system identification from the broadband signals is at 71% using an OE model. The results from simulations with single frequency excitation signals confirm the identified model. The amplitude of the reflection coefficient is below 0.05 for frequencies above 600 Hz. However, for frequencies below this threshold, an increase of the amplitude value can be observed and at frequencies towards 0, the amplitude value approaches 1. Towards lower frequencies, starting at a frequency of 2000 Hz, the phase lag approaches a value of 180°. The explanation for this behaviour is the same as in the laminar case. The behaviour of the phase curve is different than the behaviour observed in the laminar case, nevertheless the boundary shows ideal reflecting behaviour at low frequencies despite imposing a non-reflecting boundary condition.

The boundary shows reflecting behaviour for low frequencies, despite specifying a non-reflecting boundary condition.

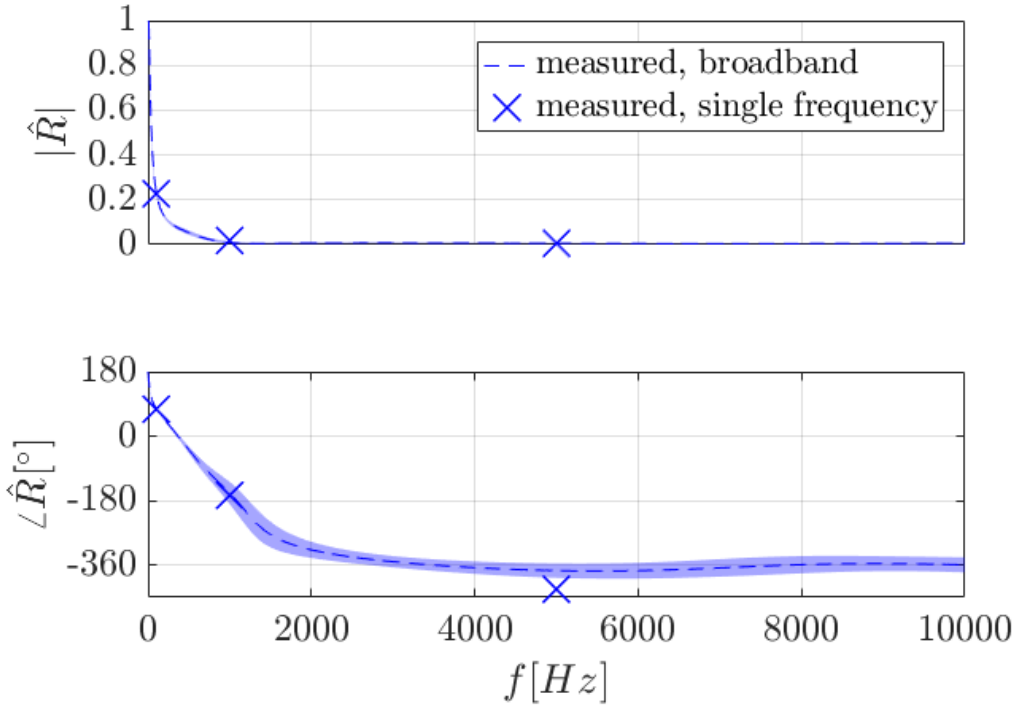

Figure 4.2: Reflection coefficient as determined at the centre of the outflow boundary for the turbulent test case.

4.2 Wall impedance

4.2.1 Laminar pipe flow with non-reflecting walls

Setup

In this chapter, laminar and turbulent test cases are investigated with the aspect of observing the influence of a non-reflecting wall section on the decrease of the magnitude of the f wave between inlet and outlet. The inflow boundary is defined as reflecting, whereas the outflow boundary is set to non-reflecting. The mean flow speed is 5 $\frac{m}{s}$. Fig. 4.3 shows the position of the non-reflecting wall section, which is used to study the effects of absorbing walls on acoustic wave propagation. The non-reflecting section of the cylinder wall represents one third of the total length.

A broadband signal is imposed at the inlet as excitation in form of velocity fluctuation. The BC an the outlet is a static pressure of 101325 Pa. Excitation signal and mesh are described in detail in Sec. 4.1.1, the mesh is taken from Jaensch et al. [10]. To calculate the transfer function between f wave at the outlet and f wave at the inlet, velocity and pressure are measured at several positions throughout the cylinder length in form of weighted face averages. The positions, where these values are observed during the simulation are shown in Fig. 4.4.

Average values over the cross section area of the pipe at inlet and outlet are used to calcu-

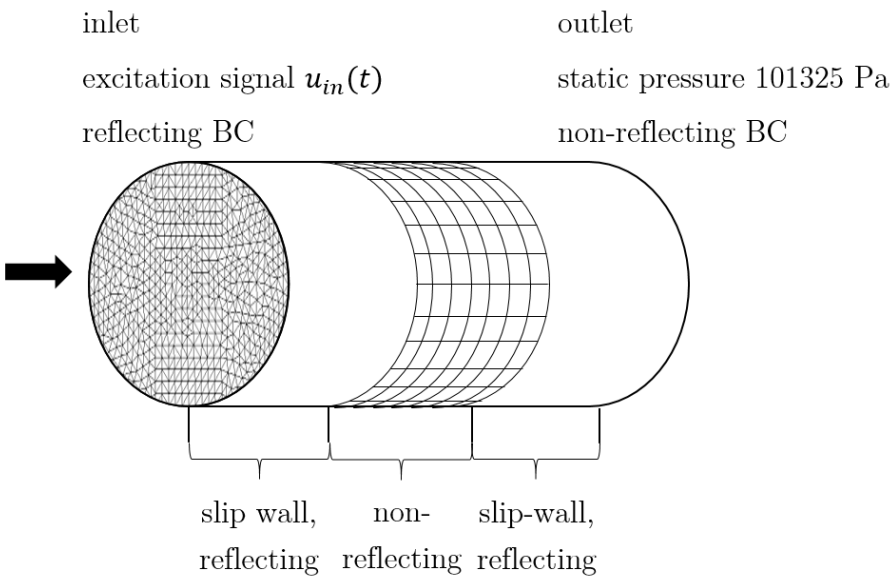

Figure 4.3: Schematic representation of the setup adapted from Jaensch et al. [10].

late the ratio of the in- and outgoing f waves in the frequency domain. The monitoring faces at the interfaces between tube sections with reflecting and non-reflecting walls are used to further examine the behaviour of f and g waves inside the domain.

Simulations with single frequency excitation are performed in order to show the accuracy of the results obtained by system identification based on the measured broadband signal of velocity magnitude and pressure on in- and outlet. Single frequency excitation is used to validate the results of the estimated transfer functions.

Results

The ratio of the amplitude with which a certain f wave leaves the domain at the outlet and enters the domain at the inlet is shown in Fig. 4.5(a) for a frequency spectrum up to 5000 Hz.

The phase is not depicted in the figure, because the section with non-reflecting walls does not change the phase at all. The acoustic propagation speed is not changed in the region of the duct that has non-reflecting walls. The amplitude of acoustic waves decreases while propagating through the duct. This decrease depends on different factors. For both, rigid and non-reflecting walls, the observed decrease in amplitude increases towards higher frequencies. The non-reflecting wall section causes a significant decrease of the propagating f wave. The good accordance between the estimated transfer functions from broadband data and the validation with excitation with one sinusoidal frequency indicates reliable estimates. An OE model is used for system identification.

Non-reflecting walls act as an acoustic damper absorbing acoustic energy even if the waves propagate parallel to these walls. Using wall impedance one could model perforated walls as it was done by [9]. The authors also stated the loss of acoustic energy.

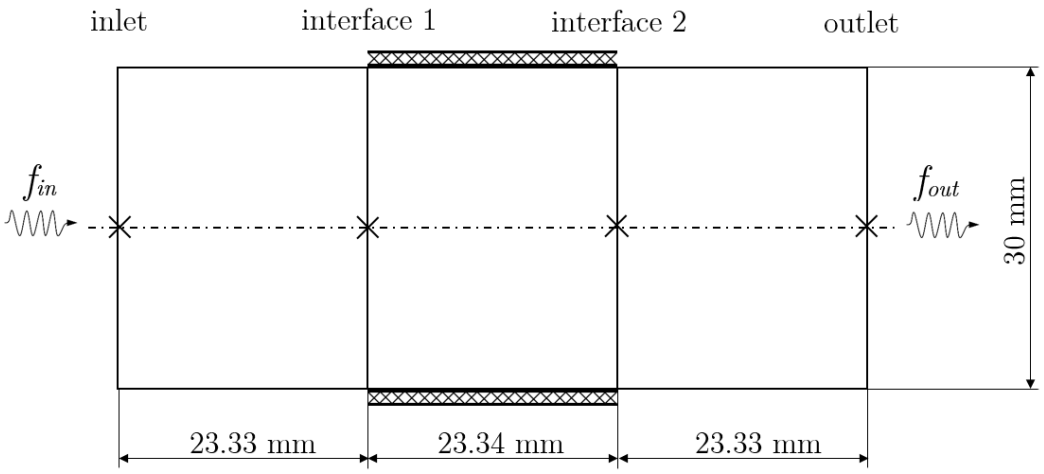

Figure 4.4: Overview over the positions where the flow information is monitored during the simulation to describe the influence of non-reflecting walls on characteristic wave propagation.

4.2.2 Turbulent pipe flow with non-reflecting walls

Setup

To examine the influence of flow conditions on the decrease in magnitude, a similar simulation setup is tested under turbulent flow conditions. Again, the influence of a non-reflecting wall section is investigated. The inlet is reflecting, the outlet is non-reflecting, the excitation signal u_{in} is imposed at the inlet. Excitation signal, turbulence parameters and mesh are described in detail in Sec. 4.3.3. The mesh is taken from Jaensch et al. [10]. The mean flow speed is 9 $\frac{m}{s}$.

Results

Fig. 4.5(b) shows the relation between the decrease of the magnitude of an f wave propagating through a duct in turbulent flow conditions. The resulting curves are plotted with 99% confidence intervals. Simulation time is 0.25 s. Additionally, single frequency analysis was performed at frequencies of 1500, 5000 and 8500 Hz to validate the results from the simulations with broadband excitation. A simulation with a single-frequency excitation signal at 80 Hz is used to validate the sudden increase towards low frequencies in the case with a non-reflecting wall section. This behaviour might be caused by the same effect as the discrepancy between imposed and measured impedance at low frequencies in Sec. 4.3.1.

The decrease in magnitude towards higher frequencies is only marginal compared to the laminar test case. Remarkably, in the case of rigid walls, the magnitude of the propagating f waves does not decrease perceptibly for frequencies below 5000 Hz. The offset between the magnitude ratio of leaving to entering f wave is relatively steady at a value of 60%.

The decline in magnitude has the same slope for laminar and turbulent case. The sudden increase of the ratio towards low frequencies in case of the non-reflecting wall section

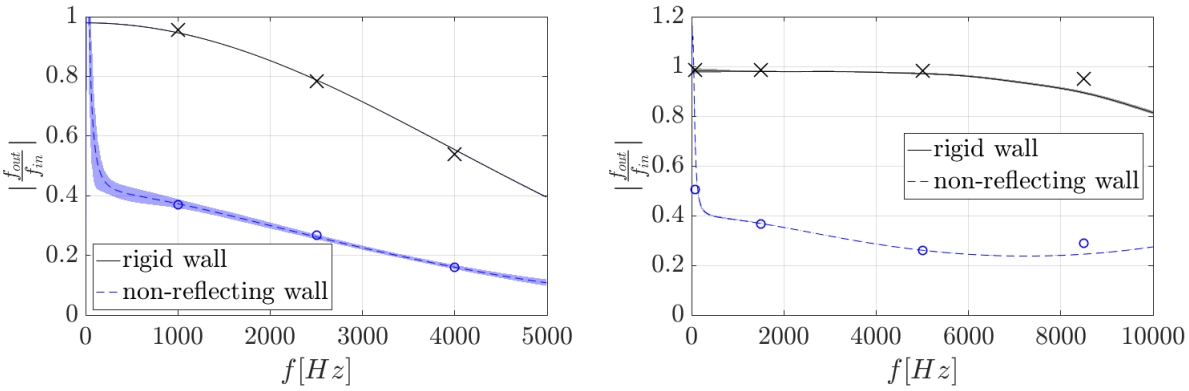

(a) laminar test case

(b) turbulent test case

Figure 4.5: Comparison of the magnitude of the transfer function $T(s) = \frac{f_{out}}{f_{in}}$ for non-reflecting and rigid (reflecting) wall for laminar and turbulent test case.

for both, laminar and turbulent test case, indicates that the amplitude of acoustic f waves entering and leaving the domain does not differ. The ratio shows the same behaviour as for reflecting walls at low frequencies. This observation is validated by single frequency excitation at 80 Hz, this is, the decrease in amplitude approaches zero for frequencies approaching 0 Hz.

The sudden increase of the ratio between outgoing and incoming wave towards low frequencies occurring at lower frequencies in the turbulent case might be due to the longer duct length in the turbulent case of 150 mm instead of 70 mm in the laminar case. The influence of the domain length on the reflection behaviour is demonstrated in Appx. E.

This allows the conclusion, that non-reflecting boundary conditions have to be handled with care in ANSYS Fluent when investigating acoustic waves at low frequencies. This observation is important for the following consideration of imposed impedance.

4.3 Imposed impedance boundary condition test cases

4.3.1 Laminar pipe flow with imposed impedance at the outlet

Setup

In this test case, we impose an impedance boundary condition at the inlet. The implementation of this test case is used to transfer the simulations of Jaensch et al. [10], who used the CFD solver *AVBP*, to another finite volume solver and thereby to show the applicability of impedance boundary conditions in a laminar flow problem with ANSYS Fluent. The same mesh as for the test case with laminar pipe flow and a non-reflecting boundary condition at the outlet is used. The inlet is defined as a standard velocity inlet. At the inlet a velocity fluctuation with a magnitude of 5% is imposed. The flow velocity is imposed by means of a broadband profile. In case of single frequency excitation, the signal is a sine wave with a mean value

of 5 $\frac{m}{s}$ at a single frequency f. The outlet of the tube is defined as a pressure outlet with a constant pressure of 101325 Pa. This is the actual pressure, whereas Fluent uses the concept of operating pressure. This concept is described in Appx. F.

An impedance boundary condition is imposed at the outlet. Tab. A.1 in Appx. A gives an overview of the coefficients of the rational polynome which is used to define an impedance boundary condition using Eq. (A.1). Therefore the poles of the rational polynomial of the reflection coefficient have to be determined. For lack of access to the input data used by Jaensch et al. [10] the reflection coefficient data is extracted from the figure depicting the Bode plot covering frequencies up to 5000 Hz. For more details about the scanning process, the reader is referred to Appx. B, where the single digitisation steps are further explained.

Results

For this laminar test case, the inlet boundary is defined as reflecting for acoustic waves, because simulations performed with a non-reflecting inlet result in fluctuations of very limited amplitude, despite the fact that the usual 5% fluctuation is imposed. Non-reflecting boundary conditions and imposed velocity interfere resulting in a lower fluctuation amplitude. A non-reflecting inlet combined with an impedance BC at the outlet leads to velocity amplitudes of less than 1% of the mean flow velocity, despite imposing a 5% excitation signal.

The results of the runs with single frequency excitation are depicted as blue crosses in Fig. 4.6.

For frequencies above 1000 Hz, the measured gain and phase values of the complex reflection coefficient at the outlet show good accordance with the imposed impedance. For lower frequencies, that is 100 and 250 Hz, the gain and even more so the phase values differ from the expected behaviour. The simulation runs with single frequency excitation were performed for a duration of at least 0.7s.

Processing the simulation results from the case with broadband excitation, the built-in Matlab function $oe(\cdot)$ leads to a model that determines a transfer function between g and f wave signals with an accuracy of 96%. The thus estimated model is shown in the figure with a 99% confidence interval is depicted as shaded area, though very small in span as a result of the high accuracy of the model. As in the case of single frequency excitation, the reflection coefficient determined by analysing the response to the broadband signal shows good accuracy for frequencies above 1000 Hz. It can be noted, that the approximated transfer function is in good accordance with the results from single frequency excitation, but differs from the imposed impedance at the outlet. This is especially the case for frequencies below 1200 Hz. Appx. D contains a summary of the multiple factors that can be excluded as cause for this offset. The observed behaviour at low frequencies can be seen as a direct result of the observed reflecting behaviour at low frequencies of boundaries which are set to non-reflecting as has been shown in Sec. 4.1.1. This can be concluded from the fact that impedance boundary conditions are implemented in ANSYS Fluent as a superposition of NSCBC and the imposed acoustic impedance. As NSCB show reflections at low frequencies, this behaviour can also be observed when investigating imposed impedance. The reflecting behaviour at low frequencies is to be considered in the same manner as for the test cases with non-reflecting boundary

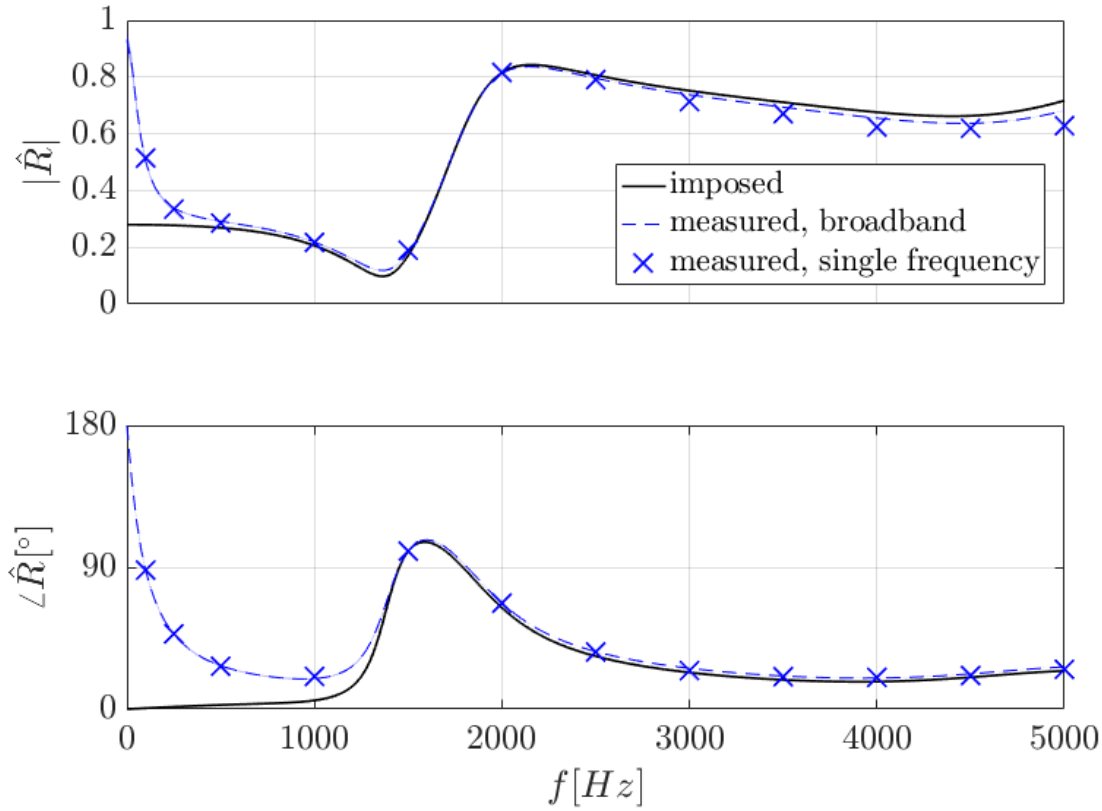

Figure 4.6: Comparison of the results obtained by single frequency and broadband excitation at the inlet of the laminar case setup, when determining the reflection coefficient at the outflow boundary. Excitation with velocity fluctuation u'_{in} at the inlet.

condition at the outlet.

4.3.2 Laminar pipe flow with imposed impedance at the outlet with non-reflecting boundary condition at the inlet

The same configuration of the laminar test case is used for another simulation, solely the broadband excitation method is changed from imposing the velocity to imposing the f wave directly. The signal is imposed using a transparent flow forcing boundary condition at the inlet, which makes it non-reflecting. At the outlet, the same impedance is imposed. Simulation time is 0.80 s with a time step size of $5 \cdot 10^{-6}$ s.

The measured reflection coefficient when directly specifying the f wave at the inlet shows the same behaviour as for the case with a velocity excitation signal. Therefore the result is not depicted. As in the first laminar test case, accordance between imposed and measured reflection coefficient above 1500 Hz is very good. However, just as for the first laminar test case, magnitude and phase of the measured reflection coefficient approach values 1 and 180°

respectively towards low frequencies. This corresponds to a standard outlet BC with zero pressure fluctuation.

Applying a non-reflecting boundary condition at the inlet results in a significant increase in computation time. For this test case, the computation time almost doubles.

4.3.3 Turbulent pipe flow with imposed impedance at the outlet

Setup

The mesh is the same as used in the setup with a non-reflecting outlet boundary condition presented in Sec. 4.1.2. At the walls, an isothermal no-slip BC is applied. The mean flow velocity is 9 $\frac{m}{s}$ with an imposed broadband fluctuation of 5% in a first run to evaluate the effect of signal-to-noise ratio, and 20% afterwards. In addition, turbulence intensity is set to 11.11%.

Given that broadband excitation is validated in the laminar test case and because of the high computational cost of the turbulent test case, the analysis is restricted to broadband excitation. The signal is composed of frequencies up to 12 kHz to ensure that the reflection coefficient can be determined for the whole spectrum. The simulation time is 1 s.

In a first simulation, the excitation is imposed at the inlet and the impedance at the outlet, which corresponds to the configuration of the laminar test case but differs from the approach taken by Jaensch et al. [10]. The reflection coefficient is determined as the ratio of g wave to f wave at the outlet. Pressure and velocity fluctuation are measured at the centre of the outlet. These signals are then used to calculate the acoustic fluctuation and finally the f and g waves. Analogously to the laminar test case, a comparison to these two signals in the frequency domain allows for determining an approximated model for the transfer function.

Results

The reflection coefficient is determined by the transfer function between g and f wave at the outlet, just as in the laminar case. This allows for determining a transfer function which shows an accordance of 76% to the two acoustic wave signals using an OE model. Fig. 4.7 shows the imposed reflection coefficient and the reflection coefficient derived from the simulation results with different excitation signal amplitudes. The curve that fits the sample points obtained by image scanning from Jaensch et al. [10] is the imposed reflection coefficient in the turbulent test case.

Whereas the phase of the complex reflection coefficient is in good agreement to the imposed impedance in case of the 5% excitation signal, the approximated amplitude determined from f and g wave differs considerably. However, the amplitude curve of the determined reflection coefficient is continuously below the imposed curve by an offset of about 0.2.

The acoustic wave signal is of the same order of magnitude as turbulent fluctuation. Therefore, the turbulent test case with velocity excitation at the inlet is repeated with a higher excitation amplitude of 20 instead of 5% of the mean flow velocity. This results in a measured reflection coefficient with good accordance to the imposed impedance. The estimate with $oe(\cdot)$ gives the best accuracy of all tested transfer function estimates. However, with an accuracy of

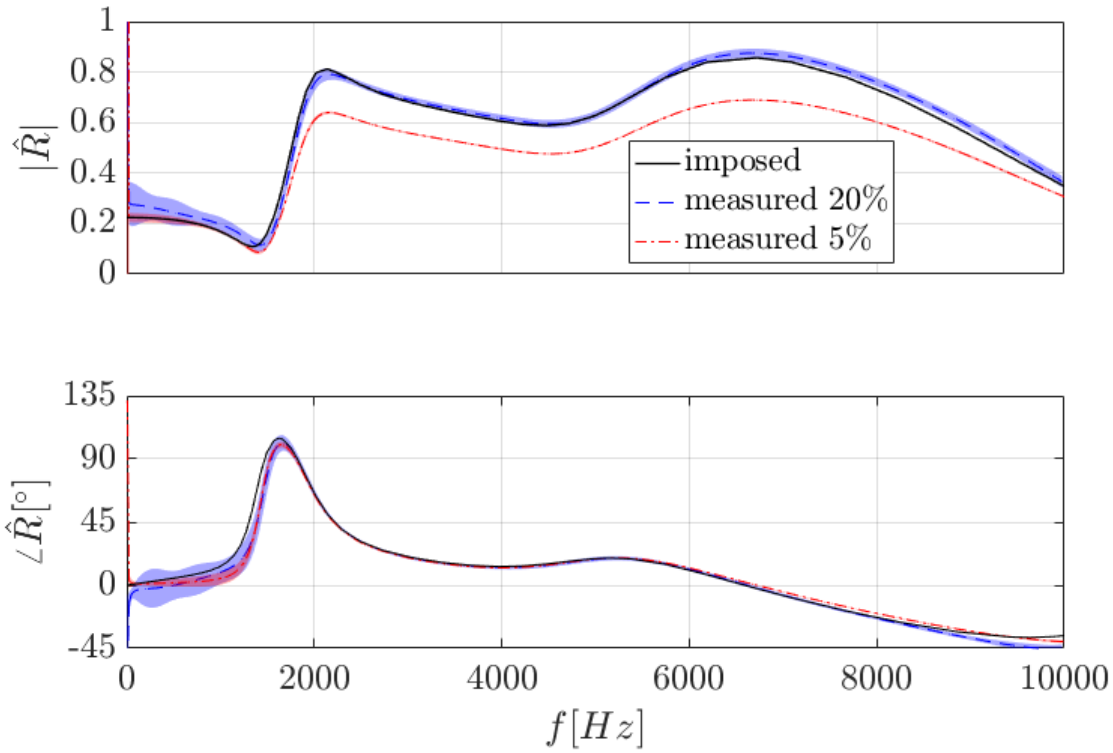

Figure 4.7: Results obtained by broadband excitation at the inlet of the turbulent case setup, when determining the reflection coefficient at the outlet boundary.

only 62%, confidence intervals are large. Thus, increasing the velocity amplitude variation of the excitation signal from 5 to 20% eliminates the offset that could be observed in the first simulation. An explanation for the better accordance between imposed and measured reflection coefficient is the higher signal-to-noise ratio. The noise is caused by turbulence. Turbulence fluctuations at the inlet were estimated to 11.11%.

Increasing the excitation amplitude variation is not an ideal solution, as this investigation is based on linearity. Another approach would be to filter the turbulence values using plane wave masking as proposed by Polifke et al. [16]. However, this concept cannot be applied in our case, because this type of boundary condition is not available in ANSYS Fluent and the types of built-in boundary conditions cannot be changed.

4.3.4 Turbulent pipe flow with imposed impedance at the inlet

Setup

In another turbulent test case, the impedance BC is imposed at the inlet, whereas the excitation signal is imposed at the outlet by means of transparent flow forcing. The imposed g wave has an amplitude variation of 20% and corresponds to a mean velocity of 9 $\frac{m}{s}$ with this amplitude variation. In this case, the reflection coefficient is determined as the ratio of f wave

to g wave at the inlet. This is the configuration used by Jaensch et al. [10]. The mesh and wall boundary conditions are the same as in for the setup presented in Sec. 4.3.3.

Results

The procedure to obtain the f and g wave at the inlet is analogous to the above described setup with excitation at the inlet. Due to the slow convergence in this simulation, the simulation time was restricted to 0.13 s. Fig. 4.8 shows the results of the second turbulent test case.

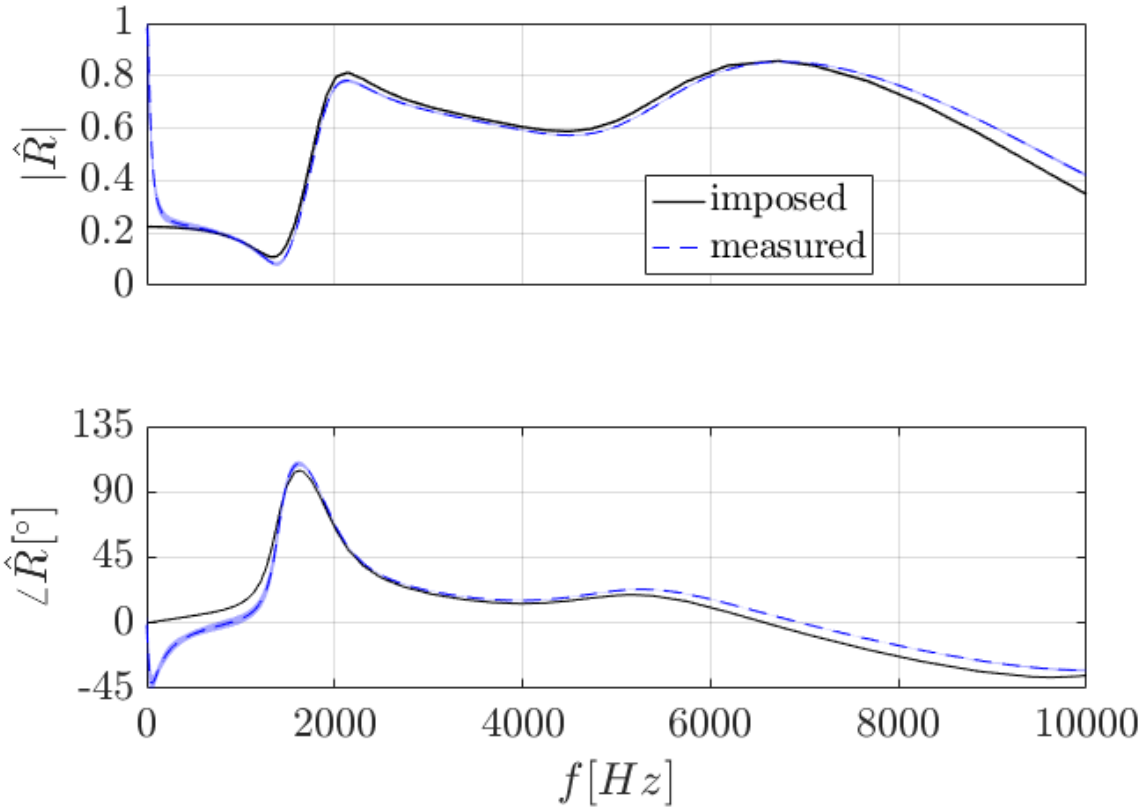

Figure 4.8: Results obtained by broadband excitation at the outlet of the turbulent case setup, when determining the reflection coefficient at the inlet boundary.

Accordance between imposed and measured reflection coefficient at the inlet is good for frequencies above 1500 Hz. For frequencies approaching zero, the amplitude of the reflection coefficient approaches a value of 1, whereas the phase approaches a value of 0°. This corresponds to a standard inlet, the imposed impedance is not being applied.

In all three test cases with imposed impedance in turbulent flow conditions, the deflection of imposed and measured amplitude of the reflection coefficient occurs at lower amplitudes, than for the investigated laminar test cases. An explanation for this behaviour could be the

longer domain length of 150 mm in the turbulent cases, compared to 70 mm in the laminar test cases. The results of an investigation of the relation between frequency-dependent behaviour and domain length can be found in Appx. E.

4.4 Combustion test cases

4.4.1 2D auto-ignition burner

Setup

This 2D test case is a simplified version of a 3D reheat combustor at high pressure developed by Zellhuber [23]. At the inflow boundary a mixture of air, fuel and first-stage combustion products enters the domain with an axial velocity of 55 $\frac{m}{s}$. See Tab. 4.1 for the species mass fractions Y_i.

Y_{CH_4} [-]	Y_{O_2} [-]	Y_{CO_2} [-]	Y_{H_2O} [-]
0.01	0.145	0.0555	0.0455

Table 4.1: Species mass fractions at the inflow boundary of the reheat combustor. Reprinted from [23].

The premixed gas ignites after a characteristic time delay due to the high inflow temperature of 1270.7 K. Turbulence intensity at the inflow is 5%. The combustion is modelled using stochastic fields, namely the progress variable approach developed by Kulkarni and Polifke [11]. In the first comparison case, the three wall sections along each side of the combustion chamber are modelled as no-slip walls with zero heat flux. In order to test the influence of non-reflecting walls on the combustion process, the two wall sections adjacent to the outflow boundary are modelled as non-reflecting walls in another test case. Non-reflecting walls are modelled as velocity inlets with a mean flow velocity of 0 $\frac{m}{s}$ with the additional condition that the surface is non-reflecting for acoustic waves.

The position of the investigated walls is indicated in Fig. 4.9. The behaviour of the walls marked with crosses is changed from reflecting to non-reflecting. The boundary conditions on the four remaining rigid wall sections are not changed. The outlet is non-reflecting and an outlet pressure of 1.8 MPa is imposed, whereas the inflow boundary is reflecting. The mesh consists of 9504 quadrilateral cells and the constant time step size is $5 \cdot 10^{-6}$ s.

The flow statistics are averaged over 13 ms to calculate mean fields. The same procedure is used to obtain mean flow fields in the setup with non-reflecting walls.

Results

The resulting mean flow fields for static pressure, heat release rate and velocity components are shown in Fig. 4.10. The figure gives the contour plots of each mean field. To facilitate comparison, the upper half of each sub-plot shows the standard case with rigid walls, and below,

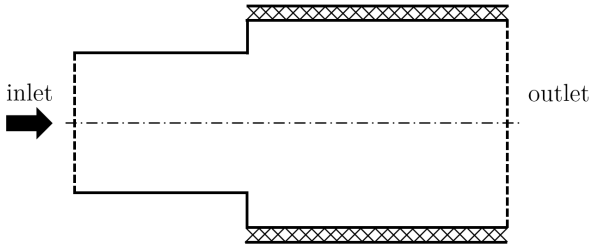

Figure 4.9: Schematic representation of the position of the non-reflecting walls for the auto-ignition test case.

mirrored at the symmetry line and with reversed y-axis, the results for the case with non-reflecting walls.

Comparing the mean flow fields of axial and tangential velocity, heat release rate and static pressure shows that the reflecting behaviour of the combustor walls is only of marginal influence on the combustion process. This observation might be due to the fact, that the flame is located relatively far from the combustor walls.

4.4.2 3D swirl burner

Setup

In order to examine the behaviour of a flame that is located closer to the combustor wall, a premixed swirl burner is investigated [6]. The swirl burner consists of several parts: At the non-reflecting inlet, a mixture of air and methane with an equivalence ratio of 0.77 enters the tube with an axial swirler with an axial velocity of 11.3 $\frac{m}{s}$ and a temperature of 293 K. Fig. 4.11 gives an overview over the components of the swirl burner model and their positions.

The walls of the tube are modelled as no-slip walls with a temperature of 293 K. At the entry plane of the tube into the combustion chamber, the inner wall of the tube extends further into the chamber. This section is called lance and is modelled in Fluent as a no-slip wall with a temperature of 600 K. The walls of the combustion chamber are modelled as standard no-slip walls in a first simulation run, and later as non-reflecting walls. The outflow boundary is non-reflecting and an outlet pressure of 101325 Pa is imposed.

In the test case with non-reflecting walls, only the combustor walls aligned with the streamwise direction are modelled as non-reflecting. Tube and lance walls remain unchanged. An under-resolved hexa mesh consisting of 653984 hexahedral cells. This under-resolved mesh is sufficient for our purposes as we do not aim at resolving the combustion dynamics in detail. The aim is to capture the main trend. LES with a constant time step size of $1 \cdot 10^{-5}$ s is used to determine the mean flow fields. The maximum CFL number is 0.9 in the swirler and 0.5 in the combustion chamber.

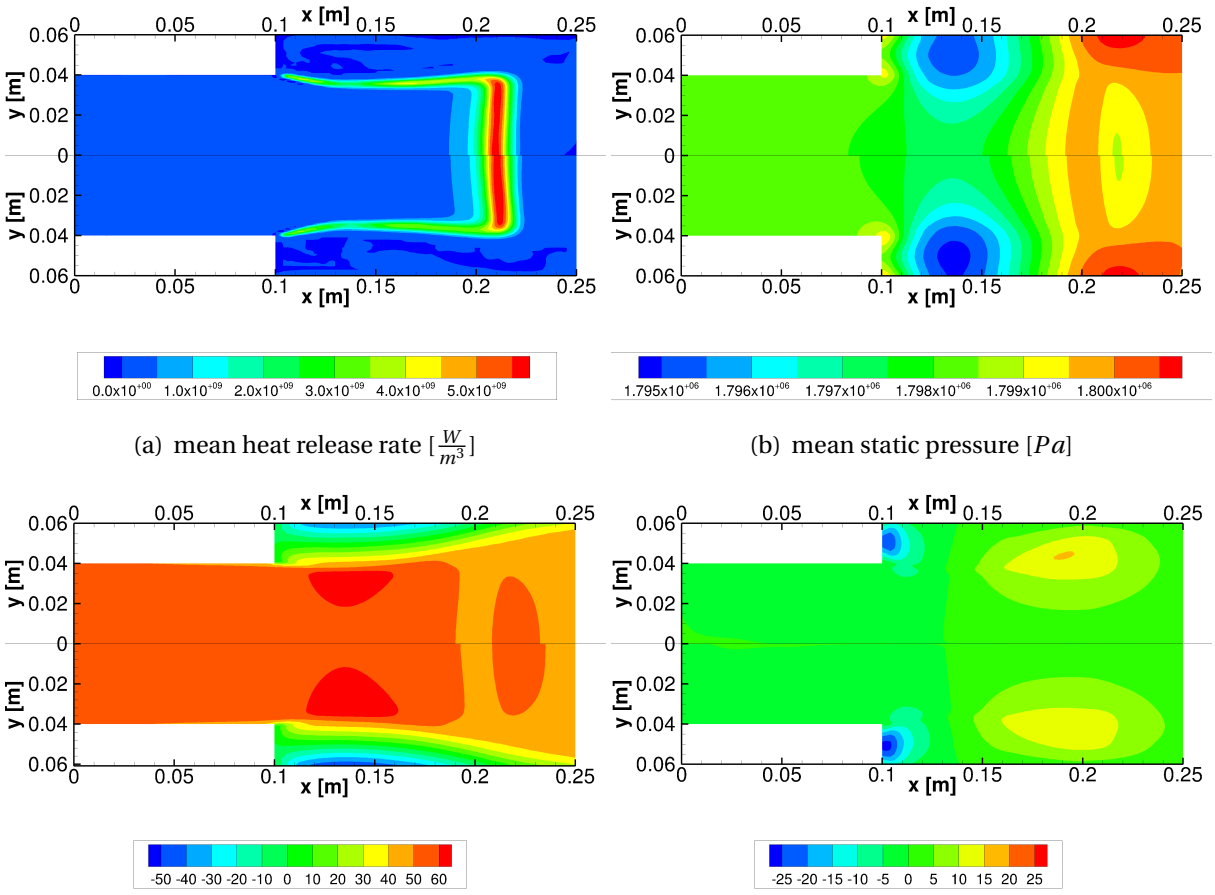

(a) mean heat release rate $[\frac{W}{m^3}]$

(b) mean static pressure $[Pa]$

(c) mean axial velocity $[\frac{m}{s}]$

(d) mean tangential velocity $[\frac{m}{s}]$

Figure 4.10: Comparison of selected mean flow fields for the auto-ignition test case with rigid walls (upper half of each subplot) and with non-reflecting walls (lower half of each subplot).

Results

Fig. 4.12 gives the contour plots of selected mean fields in the middle cut plane of the combustor. The section of the tube upstream of the swirler is cut off as this section is not relevant for our investigations.

The comparison of the mean flow fields of axial and tangential velocity, heat release rate and static pressure for the setups with rigid and non-reflecting walls shows that the reflecting behaviour of the combustor walls does not perceptibly influence the combustion process. The position of the flame, which is located close to the walls, does not change. Together with the observation from the 2D combustion test case, this allows the conclusion that non-reflecting walls can be simulated as zero mean flow inlets with NSCBC.

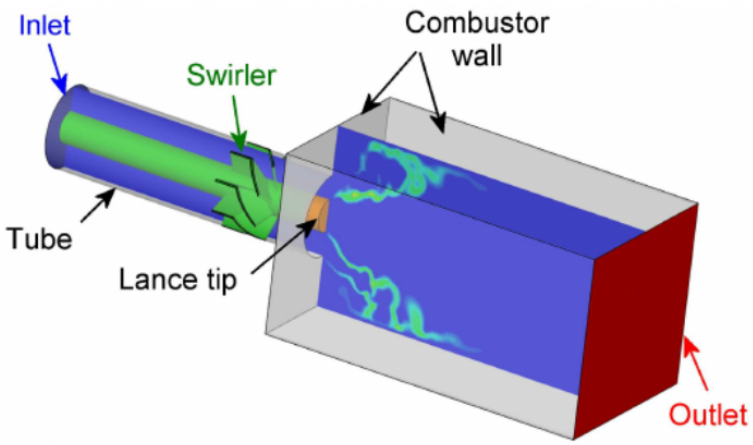

Figure 4.11: Schematic representation of the parts constituting a model of a swirl burner used as 3D test case. Reprinted from [14].

4.4.3 3D swirl burner with transverse excitation

Setup

The model of the swirl burner as described in the previous section is used for another simulation setup. All walls are standard walls. Except two opposite walls: on the upper wall of the combustion chamber, transparent flow forcing is used to impose a transverse acoustic wave entering the domain. The amplitude of the acoustic wave is equivalent to a pressure fluctuation of 100 Pa. This yields a sufficient signal to noise ratio at the lower wall. A broadband signal with high power spectral density up to 10 kHz is used as excitation signal.The estimated model from broadband identification is validated using a simulation setup with single frequency excitation at 100, 1000 and 5000 Hz. The bottom wall of the combustion chamber is set to non-reflecting. Turbulence intensity at the non-reflecting walls is set to zero. The rest of the setup is not changed, namely the mesh, the other boundary conditions and the combustion parameters. A time step size of $2.5 \cdot 10^{-6}$ s is chosen and the simulation time is 0.03 s for all setups. The time step size was decreased due to stability problems.

Following the definition of plane acoustic waves in stream-wise direction in Eq. (2.25), transverse acoustic waves are defined based on the transverse velocity v as

$$\begin{aligned} f^T(x,t) &= \frac{1}{2}\left(\frac{p'(x,t)}{\overline{\rho}\,\overline{c}} + v'(x,t)\right) \\ g^T(x,t) &= \frac{1}{2}\left(\frac{p'(x,t)}{\overline{\rho}\,\overline{c}} - v'(x,t)\right), \end{aligned} \tag{4.2}$$

where the superscript T marks the transverse wave. The f^T wave propagates in the direction, in which v is defined positive. The g^T wave propagates in the reverse direction. Fig. 4.13 schematically shows the transverse acoustic waves at top and bottom wall of the combustion chamber.

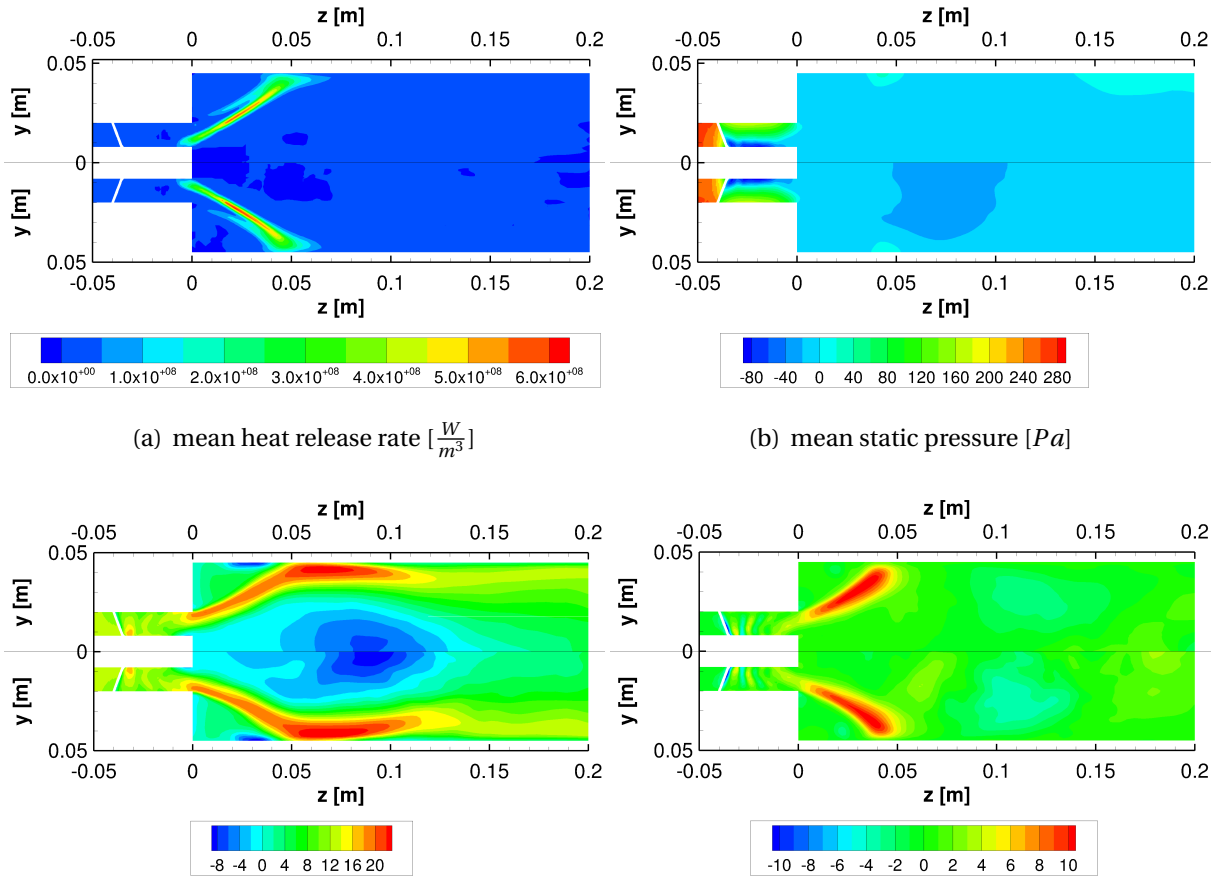

(a) mean heat release rate $[\frac{W}{m^3}]$

(b) mean static pressure $[Pa]$

(c) mean axial velocity $[\frac{m}{s}]$

(d) mean tangential velocity $[\frac{m}{s}]$

Figure 4.12: Comparison of selected mean flow fields in the middle cut plane of the 3D swirler with rigid walls (upper half of each subplot) and with non-reflecting combustion chamber walls (lower half of each subplot).

At several points at the bottom wall of the combustion chamber, covering its whole breadth and length, the actual reflection coefficient is determined as the transfer function

$$\hat{R} = \frac{f_b^T}{g_b^T}, \tag{4.3}$$

where the subscript b indicates the bottom wall as the position of evaluation, whereas t would indicate the top wall. The reflection coefficient is evaluated at points only, because the combustion process causes large temperature and thus sound speed gradients along the bottom combustion chamber wall in axial direction. Local wall temperatures differ to such an extent, that averaging over the bottom wall is not possible. Therefore, the characteristic density and sound speed values at each point are used to calculate the acoustic waves.

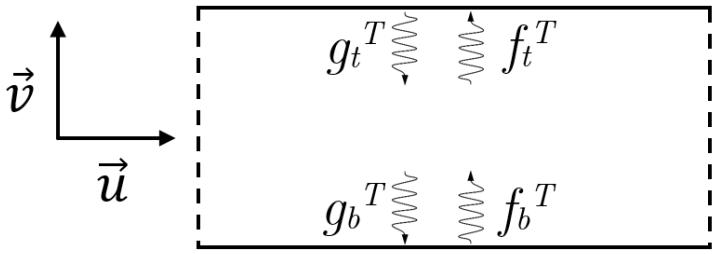

Figure 4.13: Schematic representation of transverse waves at top (t) and bottom (b) wall of the combustion chamber.

Results

Fig. 4.14 schematically shows the positions where point data is monitored during the simulation.

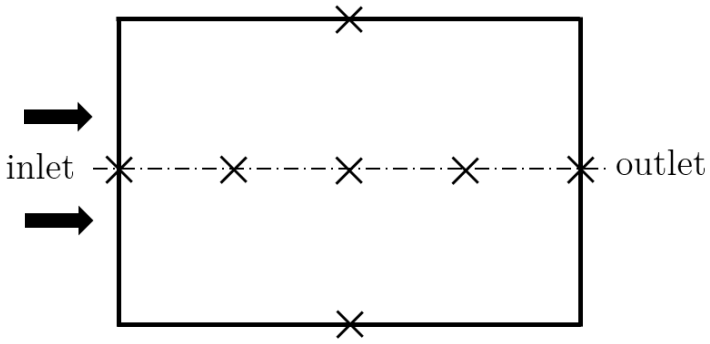

Figure 4.14: Schematic top view of the bottom combustion chamber wall with the positions where the reflection coefficient is determined.

The reflection coefficient at the centre point of the lower combustion chamber wall as determined from simulation data is shown in Fig. 4.15. The reflection coefficient is shown at this point, as the results obtained for all investigated positions at the bottom wall do not differ significantly. At this position, the sound speed $\overline{c}$ is 825 $\frac{m}{s}$ and the density $\overline{\rho}$ is 0.188 $\frac{kg}{m^3}$.

The measured reflection coefficient is below 0.1 for frequencies above 500 Hz. Below this threshold, the amplitude approaches a value of 1, and the phase a value of 180°. The phase shift of 180° for frequencies approaching zero and an amplitude of the reflection of 1 represent a perfectly reflecting wall. The accuracy of the estimated model is 75% using an OE model. The results obtained from simulations with single frequency excitation at the upper wall validate the identified system.

The mean fields of heat release rate, static pressure and axial and tangential velocities do not show a perceptible change compared to the setup with non-reflecting combustor walls and without transverse excitation.

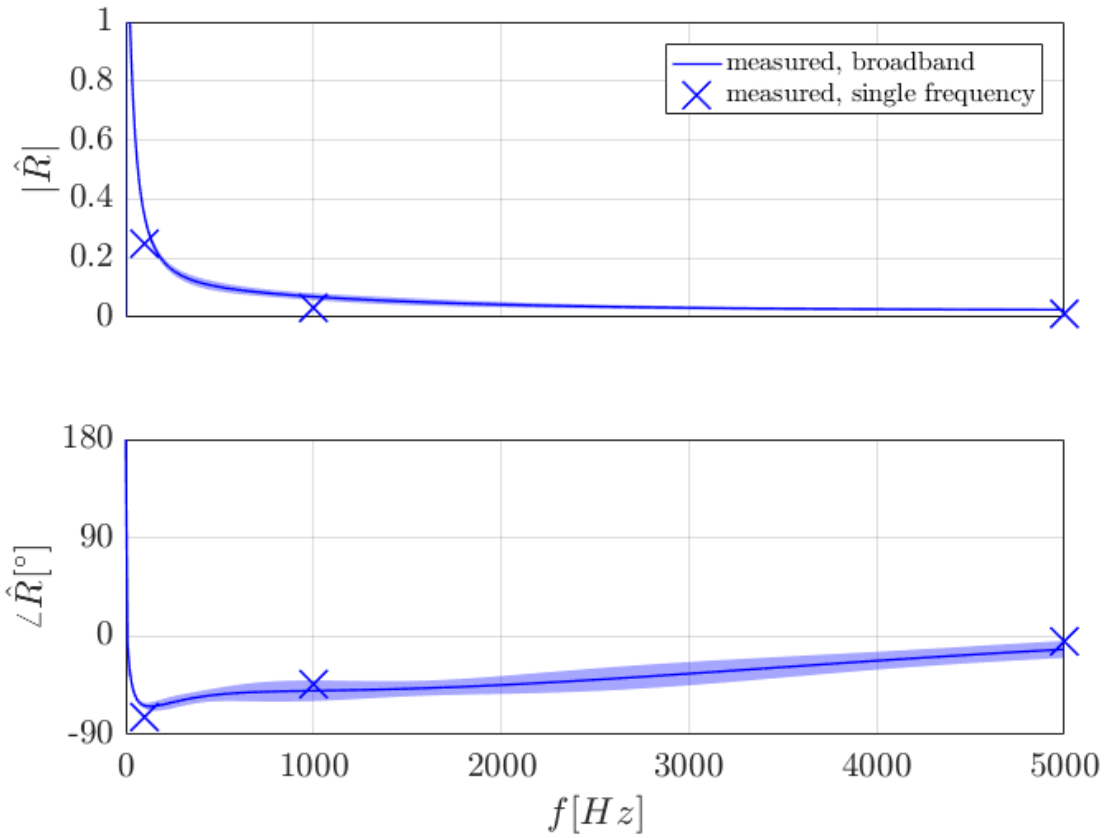

Figure 4.15: Determined reflection coefficient at the centre of the bottom wall of the combustion chamber.

In conclusion, a non-reflecting boundary condition with zero mean flow in ANSYS Fluent indeed results in non-reflecting walls. However, the reflecting behaviour depends on the frequency of the incoming wave. At low frequencies the reflection coefficient approaches that of a rigid wall. This is due to the restriction for non-reflecting walls explained in Sec 2.3.1 and Sec. 3.2. This limitation has to be kept in mind when modelling mufflers as non-reflecting walls.

5 Conclusion and outlook

Conclusion

Non-reflecting walls modelled by NSCBC are reflecting at low frequencies. The reason is an additional constraint to prevent the mean fields from drifting. Non reflecting behaviour at low frequencies improves when the characteristic domain length is larger.

An impedance boundary condition is a superposition of a non-reflecting boundary condition and a transformation in form of a convolution integral with the imposed impedance. Therefore we get wrong results for low frequencies where the non-reflecting boundary conditions do not work.

Non-reflecting walls do not influence the flame position of a stable configuration. Non-reflecting walls were validated with transverse excitation. There is the same problem at low frequencies as for inlet and outlet boundaries.

Outlook

One could try to find an optimal set of parameters for better results at low frequencies. However, as this approach is associated with restrictions, we recommend to use plane wave masking in further studies as this would allow for higher identification quality and lower excitation amplitudes. Furthermore, the investigation of the interaction of non-reflecting walls and boundary layer development is still outstanding. This should include an evaluation of the influence on the reattachment point. Future research should treat a test case with self excited transverse oscillations in which the instability is damped using non-reflecting walls.

Appendices

A Specifying an impedance boundary condition in Fluent

	α_l [-]	β_l [-]	B_l [-]	C_l [-]	λ_k [-]	A_k [-]
complex pole 1	7969.8	32494	-1728	1958.5	–	–
complex pole 2	2271	11306	-1217.2	1083.3	–	–
real pole 1	–	–	–	–	151890	160310
real pole 2	–	–	–	–	17640	-7261.1

Table A.1: Coefficients of the rational polynome describing the reflection coefficient in the frequency domain imposed as boundary condition at the pressure-outlet in the laminar case.

	α_l [-]	β_l [-]	B_l [-]	C_l [-]	λ_k [-]	A_k [-]
complex pole 1	28979	59348	-30866	-25842	–	–
complex pole 2	9632.4	33392	-3074	3865.8	–	–
complex pole 3	2074	11694	-832.81	1115.8	–	–
real pole 1	–	–	–	–	230850	367620
real pole 2	–	–	–	–	31525	-37482

Table A.2: Coefficients of the rational polynome describing the reflection coefficient in the frequency domain imposed as impedance boundary condition in the turbulent case.

The coefficients can be used in Fluent following the nomenclature of the Impedance Boundary Condition Toolbox in the Fluent user manual [4] using the formulation

$$\hat{R}(s) = D + \sum_{k=1}^{N_1} \frac{A_k}{(s+\lambda_k)} + \sum_{l=1}^{N_2} \left(\frac{B_l + iC_l}{(s+\alpha_l - i\beta_l)} + \frac{B_l - iC_l}{(s+\alpha_l + i\beta_l)} \right). \tag{A.1}$$

B Digitisation with Matlab

For the digitisation of the figure, the functions were sampled at 30 points and the collected data points were used to make a least-square fit. The determined function was transformed into a model in the frequency domain and finally into a rational polynomial.

The frequency-dependent reflection coefficient at the boundaries are imposed in both, laminar and turbulent test cases. Due to restricted access to the raw data of Jaensch et al. [10], the imposed impedance boundary coefficient is derived from their figure in by means of data digitisation. Therefore, the built-in Matlab function $digitize2$ is used to digitise the magnitude and phase values at 28 equidistant points on the curve between 0 and 5000 Hz. The procedure is analogous for their figure depicting amplitude and phase curve for the turbulent case. Again, the curve of the imposed reflection coefficient is scanned. For the figure of the turbulent case, 26 points are used.

The digitised samples with magnitude and phase value are used to determine a fit. For this purpose, the built-in function $rationalfit$ is used. To avoid overfitting, the number of poles is limited to 6, which shows very good accordance with the original curve from Jaensch et al. [10]. For the fit of the curve of the turbulent case, the number of poles is set to 8, which allows to fit the curves smoothly for magnitude and phase curves. The resulting curve fits are rational functions. For the turbulent case, the derived complex rational function is

$$\begin{aligned}\hat{R}(s) = &\frac{367620}{s+230850} + \frac{-37482}{s+31525} + \\ &\frac{-30866-25842i}{s+28979-59348i} + \frac{-30866+25842i}{s+28979+59348i} + \\ &\frac{-3074+3865.8i}{s+9632.4-33392i} + \frac{-3074-3865.8i}{s+9632.4+33392i} + \\ &\frac{-832+1115i}{s+2074.4-11694} + \frac{-832-1115i}{s+2074.4+11694},\end{aligned} \tag{B.1}$$

where $s = \omega i = 2\pi f i$. For the laminar case, the complex function describing the reflection coefficient in the frequency domain is

$$\begin{aligned}\hat{R}(s) = &\frac{160310}{s+151890} + \frac{-7261.1}{s+17640} + \\ &\frac{-1728+1958.5i}{s+7969.8-32494i} + \frac{-1728-1958.5i}{s+7969.8+32494i} + \\ &\frac{-1217.2+1083.3i}{s+2271-11306i} + \frac{-1217.2-1083.3i}{s+2271+11306i}.\end{aligned} \tag{B.2}$$

The derived real and complex pole and zero values can be implemented in ANSYS Fluent

after a slight change in notation, namely the convention of signs.

Fig. B.1 shows the scanned data points and the fitted rational function representing the reflection coefficient at the outlet in the laminar case.

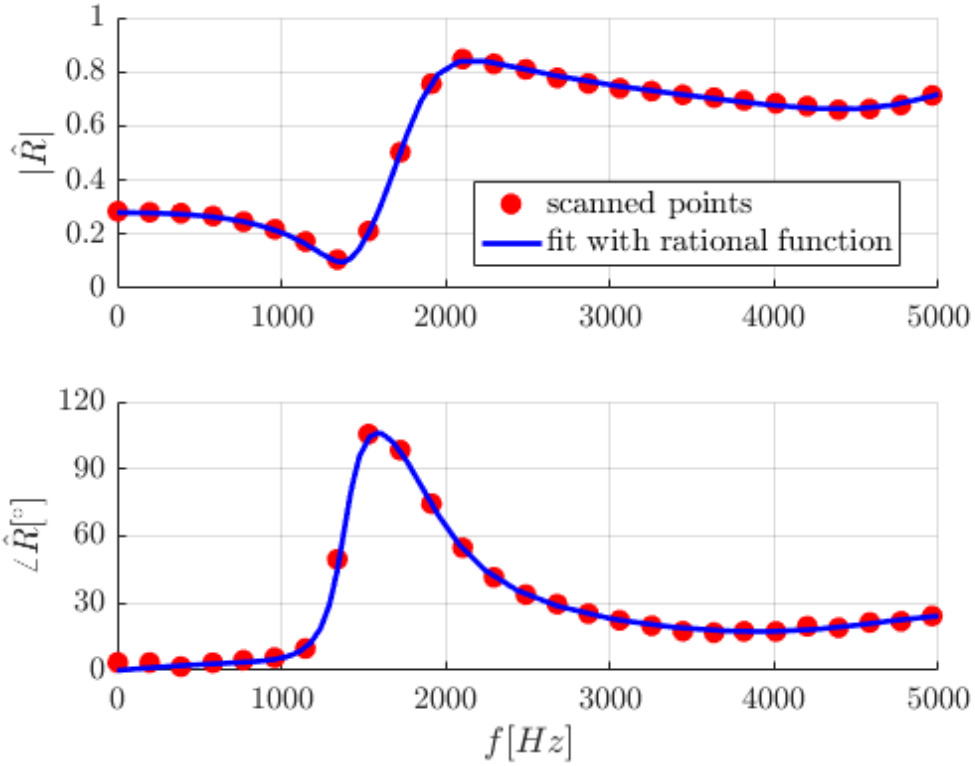

Figure B.1: Comparison of sampled data from input used by Jaensch et al. [10] and the least-square fit with 6 poles to be used for imposing the impedance in the laminar test case. Following Jaensch et al. [10].

Comparing the sampled data from the original figure and the fitted function shows very good accordance for magnitude and phase data.

The scanned data points and the fitted rational function representing the reflection coefficient at the outlet in the turbulent case are shown in Fig. B.2.

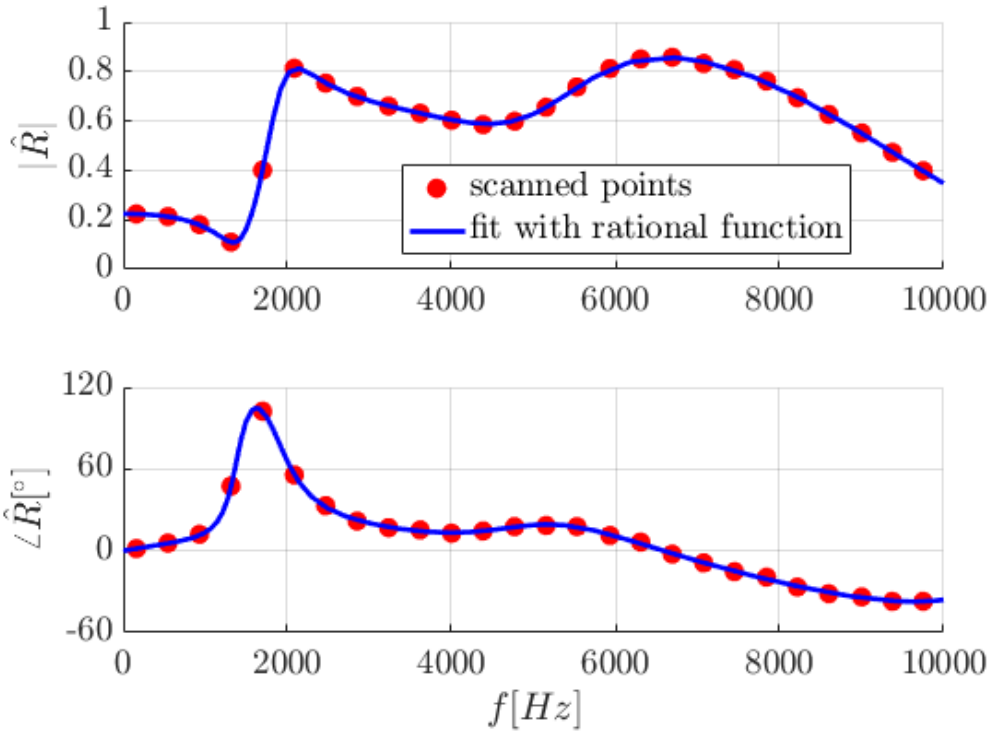

Figure B.2: Comparison of sampled data from input and the least-square fit with 8 poles for the impedance BC of the turbulent case. Following Jaensch et al. [10].

C Post-processing of Fluent data

When running a simulation, the flow velocity and the static pressure of the flow on the in- and outlet are monitored and saved. For every time step, the velocity and pressure values of the converged solution are saved for the center of the in- and outflow boundary and in form of the mass-weighted average for the velocity, and the area-weighted average for the pressure on these surfaces. The values on the centreline are used to validate the data calculated from the averaged values. Averaged velocity magnitude and pressure data are then processed for the boundary face, on which a reflection coefficient has been imposed and is to be compared with the simulation data. At first, the mean values in time of these mass-flow averaged velocity magnitude and area-weighted pressure are determined for the complete simulation time on the velocity-inlet or pressure-outlet of interest. Then, the fluctuation of velocity and pressure is determined as the difference between the value of the flow variable at each time step, and the determined mean value over the simulation time. Using the mean density ρ and a mean speed of sound c of the mean flow field, the vectors containing the amplitudes of the acoustic f and g wave for each time step are determined as

$$\begin{aligned} f &= \frac{1}{2}\left(\frac{p'}{\overline{\rho c}} + u'\right) \\ g &= \frac{1}{2}\left(\frac{p'}{\overline{\rho c}} - u'\right), \end{aligned} \tag{C.1}$$

applying Eq. (2.26) to vectors containing velocity amplitude and pressure fluctuation value for every time step. Further processing steps are different for analysing simulation results with single frequency and broadband excitation.

Broadband signal processing

The first 0.04 s of the signals are cut off to avoid transient effects. This interval proved sufficient to develop regular flow in the whole domain. The restricted time interval of f and g waves, together with the constant time step size is then combined to an $iddata$ object in Matlab. The position at which the reflection coefficient is to be determined defines which wave amplitude is the input and which is the output of this object. The final step consists of estimating a transfer function between in- and output of this system. The different approaches of estimating transfer functions are presented in Sec. 2.5. The accuracy of the thus estimated model is then determined by comparing the output of the model with the measurement data.

Single frequency signal processing

To determine the reflection coefficient from simulation data in case of single frequency excitation, the first 0.05 s of the $\vec{f}$ and $\vec{g}$ vectors are cut off to ignore transient processes. The remainder of the vectors containing wave amplitude data, together with the corresponding time vector $\vec{t}$ are cut to a length that corresponds to a multiple of an oscillating period of the excitation signal. A fast Fourier transformation is performed with these signals. In the frequency domain, the transfer function between $F(\omega)$ and $G(\omega)$ or vice-versa is determined as the ratio between the in- and outgoing wave on the boundary face of interest. The thus determined magnitude and phase is then compared to the values of gain and phase of the imposed reflection coefficient at the same frequency. Single frequency excitation is used to validate the identified model.

D Tentatives to improve non-reflecting behaviour at low frequencies

D.1 Relaxation factors: parameter study

Fig. D.1 shows the measured reflection coefficient on the outflow boundary for the laminar test case with velocity excitation on the inlet. The time step size is $1 \cdot 10^{-5}$ s for all cases, with a total simulation time of 0.7 s. The first 0.04 s of the measured signals are cut off. The accuracy of the models estimated from the resulting f and g wave signals is above 80% in each case.

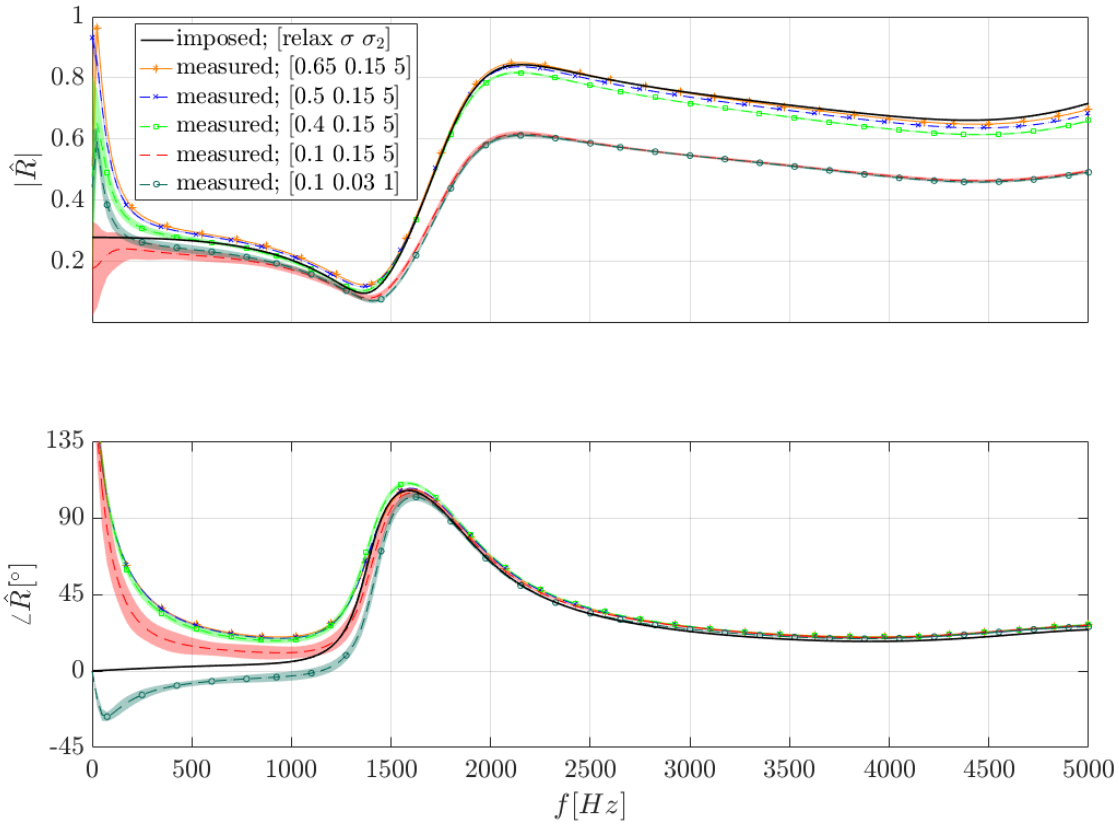

Figure D.1: Measured reflection coefficients for different relaxation factors $relax$, compared to the imposed impedance. One test case with variation of the relaxation factors σ and σ_2.

Apparently, better accordance of the measured reflection coefficient magnitude at low frequencies can only be achieved using a low relaxation factor of $relax = 0.1$. However, this is only possible at the cost of a significant offset at higher frequencies.

The figure implies that the phase curve of the measured reflection coefficient does not depend on the relaxation factor $relax$. Decreasing the relaxation factors σ and σ_2 to a fifth of the default value leads to a resulting phase curve with lower phase values than in the preceding test cases. This suggests, that σ values in between would achieve good accordance between imposed and measured reflection coefficient. However, exclusively with $relax$ values which have proven to result in a large offset at high frequencies. This conclusion, together with the observation that calculation time is considerably larger for low relaxation factor values, are the reason why all test cases in this thesis are simulated with the default relaxation factors for non-reflecting boundaries. This is

$$\begin{aligned} relax &= 0.5, \\ \sigma &= 0.15, \\ \sigma_2 &= 5. \end{aligned} \tag{D.1}$$

D.2 Poles of impedance function

In order to determine, whether the diverging behaviour at low frequencies is a result of the function describing the imposed impedance in the form of a sum of rational polynomials, another impedance function is imposed on the outlet of the laminar test case. The inlet is reflecting and the inflow velocity is imposed. The imposed reflection coefficient in the frequency domain is

$$\hat{R}(s) = \frac{2457 + 873.18i}{s + 2785.1 - 13296i} + \frac{2457 - 873.18i}{s + 2785.1 + 13296i}. \tag{D.2}$$

The imposed impedance is shown in Fig. D.2, compared to the reflection coefficient as obtained from simulation data with 99% confidence interval, which is shown as a shaded region. In addition to the estimated model derived from broadband excitation, a test case using single frequency velocity excitation is performed to validate the accuracy of the estimated model at a frequency of 100 Hz.

Simulation time is 0.30 s with a constant time step size of $1 \cdot 10^{-5}$ s. The reflection coefficient is estimated from f and g wave signals using $tfest(\cdot)$ with an accuracy of 96%, which accounts for the relatively small 99% confidence intervals for magnitude and phase.

Towards low frequencies, imposed and measured magnitude of the reflection coefficient diverge considerably, which is confirmed by the results from single frequency analysis. However, it can be observed that an imposed phase value of 180° at frequencies approaching zero, is in accordance to simulation results.

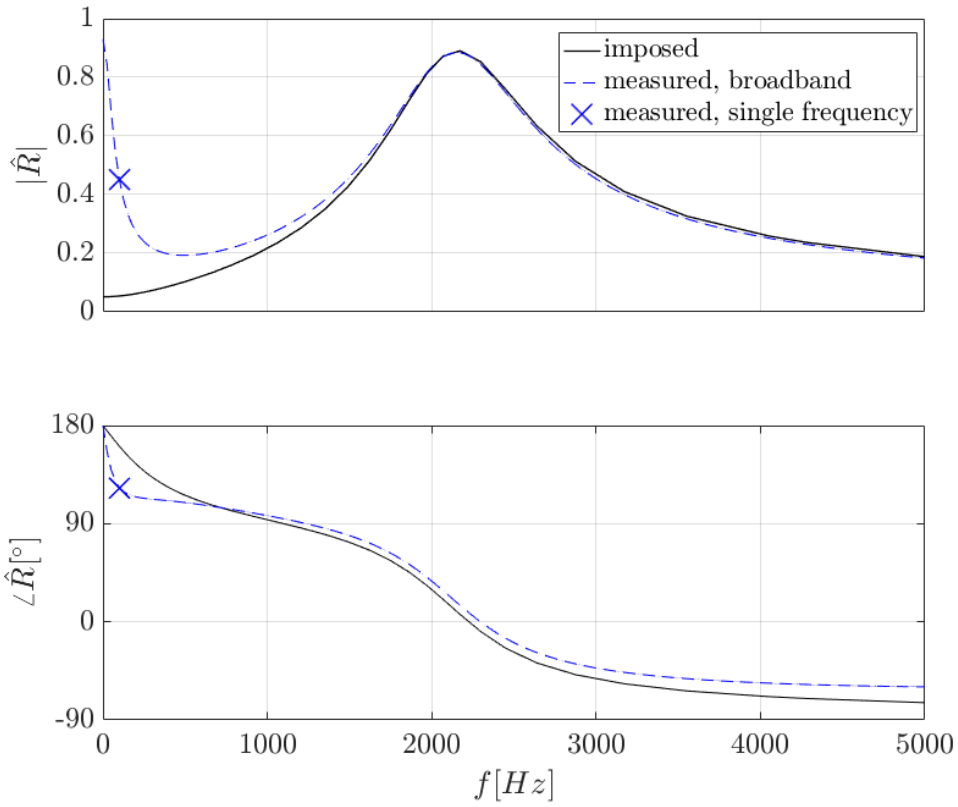

Figure D.2: Imposed and measured reflection coefficient on the outlet for the laminar test case with an impedance with one complex conjugate pole pair.

D.3 CFL number

Fig. D.3 shows a comparison of the results obtained when using different time step sizes. The simulation of the laminar test case with velocity excitation on the inflow boundary was performed for a CFL number of 3.36, which is decreased to 0.84 by dividing the original time step size of $1 \cdot 10^{-5}$ s by four. The simulation time for all test cases is set at 0.7 s. In the case of the simulations with high CFL number, a broadband signal is used for excitation. For the simulations with low CFL number, single-frequency excitation signals at frequencies of 100 and 3000 Hz are used. All the simulations are repeated for relaxation factors $relax$ of 0.4 and 0.1.

Comparing the results allows to conclude that performing simulations at the above mentioned CFL numbers gives results with negligible differences. Therefore, all further simulations of the laminar test case are calculated with the higher CFL number. This allows to gather more low frequency data at the same computational cost without significantly impairing the accuracy of the results.

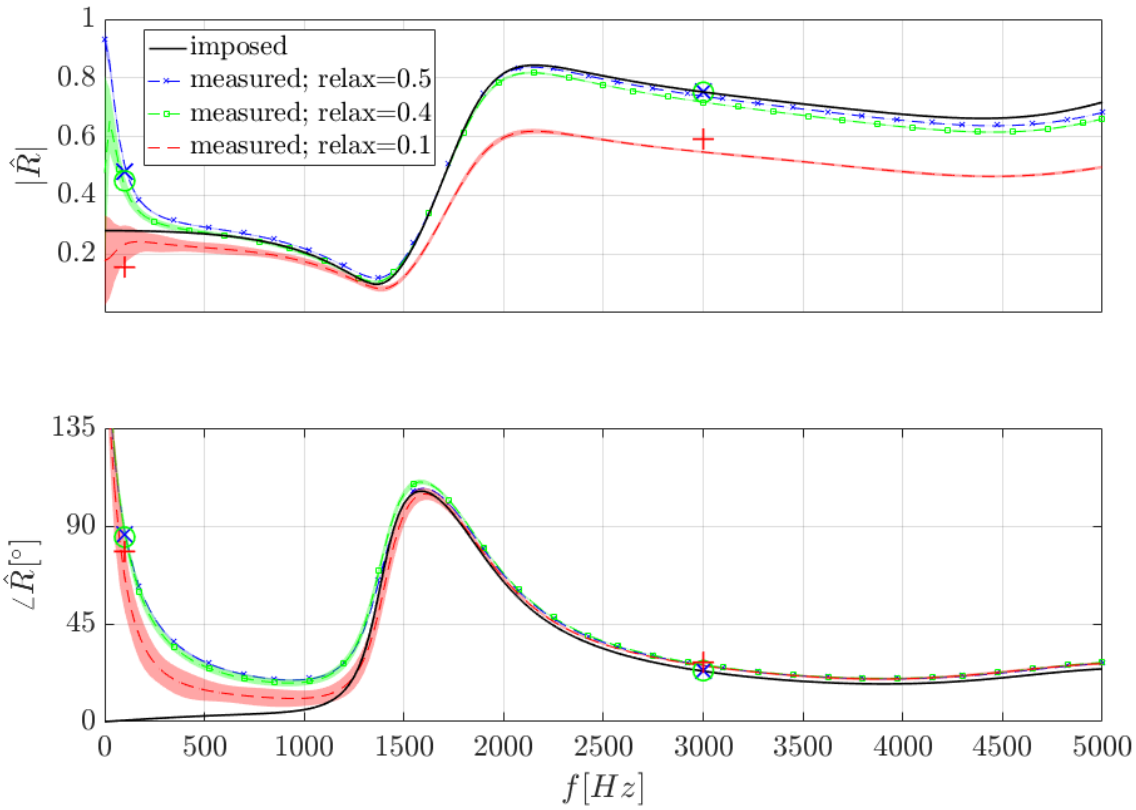

Figure D.3: Reflection coefficient estimated from broadband data from laminar test case with $CFL = 3.36$ (continuous lines with small markers) compared to results from single frequency excitation with $CFL = 0.84$ (large markers) for three different relaxation factor values.

D.4 Power spectral density

Low power spectral density of the f and g wave signals calculated from monitored velocity and pressure on the outlet during simulation is not the case. Fig. D.4 shows the single-sided power spectral density for the laminar test case with a simulation time of 0.90 s, a CFL number of 3.36 and the default value of 0.5 for the relaxation parameter $relax$.

As the intensity at low frequencies is comparable to that at the rest of the examined spectrum, power spectral density can be excluded as cause for the deviation of the measured from the imposed reflection coefficient at low frequencies.

D.5 Laminar versus turbulent flow

The influence of the relaxation factor $relax$ under turbulent flow conditions is similar to the laminar test case, as the comparison in Fig. D.5 clearly shows. This is the second turbulent test case, with excitation on the outlet with the upstream propagating wave g_{in}.The outlet is

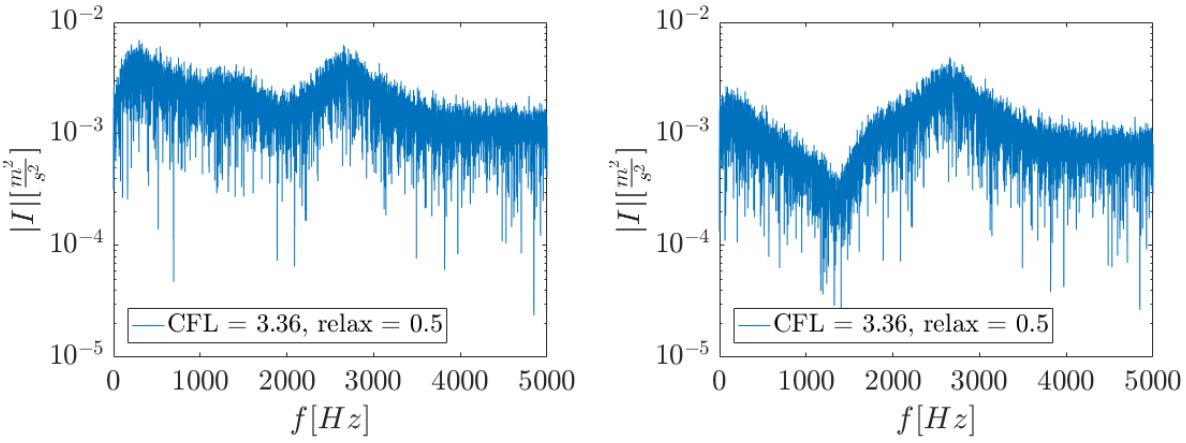

(a) f wave signal

(b) g wave signal

Figure D.4: Power spectral density (single-sided amplitude spectrum) of f and g wave signals as calculated from velocity and pressure fluctuation for the laminar test case.

non-reflecting and the impedance is imposed on the inlet.

The reflection coefficient determined from the results of the simulation with lower relaxation factor show a significant offset of the magnitude value over the whole spectrum. Solely the behaviour at low frequencies is closer to the imposed impedance than for the case with default relaxation parameter value.

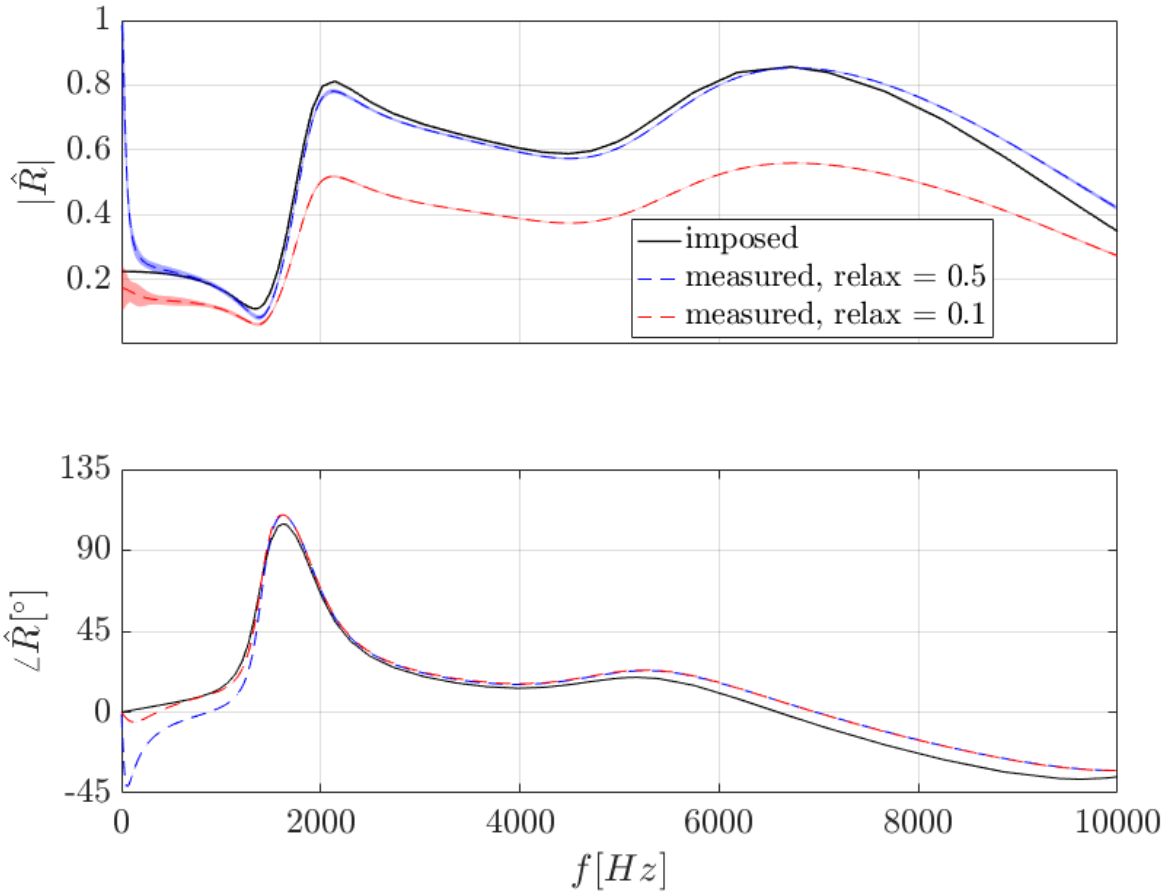

Figure D.5: Comparison of the estimated and imposed reflection coefficient on the inlet for the turbulent test case with transparent flow forcing boundary condition on the outlet.

E Variation of duct length

In order to examine the influence of the duct length on the measured reflection coefficient, the laminar test case is compared with similar laminar test cases, in which the domain length was changed from 70 to 35 and 140 mm respectively. The inlet is reflecting, whereas the impedance from the standard laminar test case is imposed on the outlet. A velocity fluctuation of 5 % for the 35 and 70 mm cases, and of 20 % for the 140 mm case is used as excitation signal on the inlet. The walls are modelled as slip walls. Simulation time is 200 ms for each case. Fig. E.1 shows imposed and measured reflection coefficient on the outlet for all three test cases.

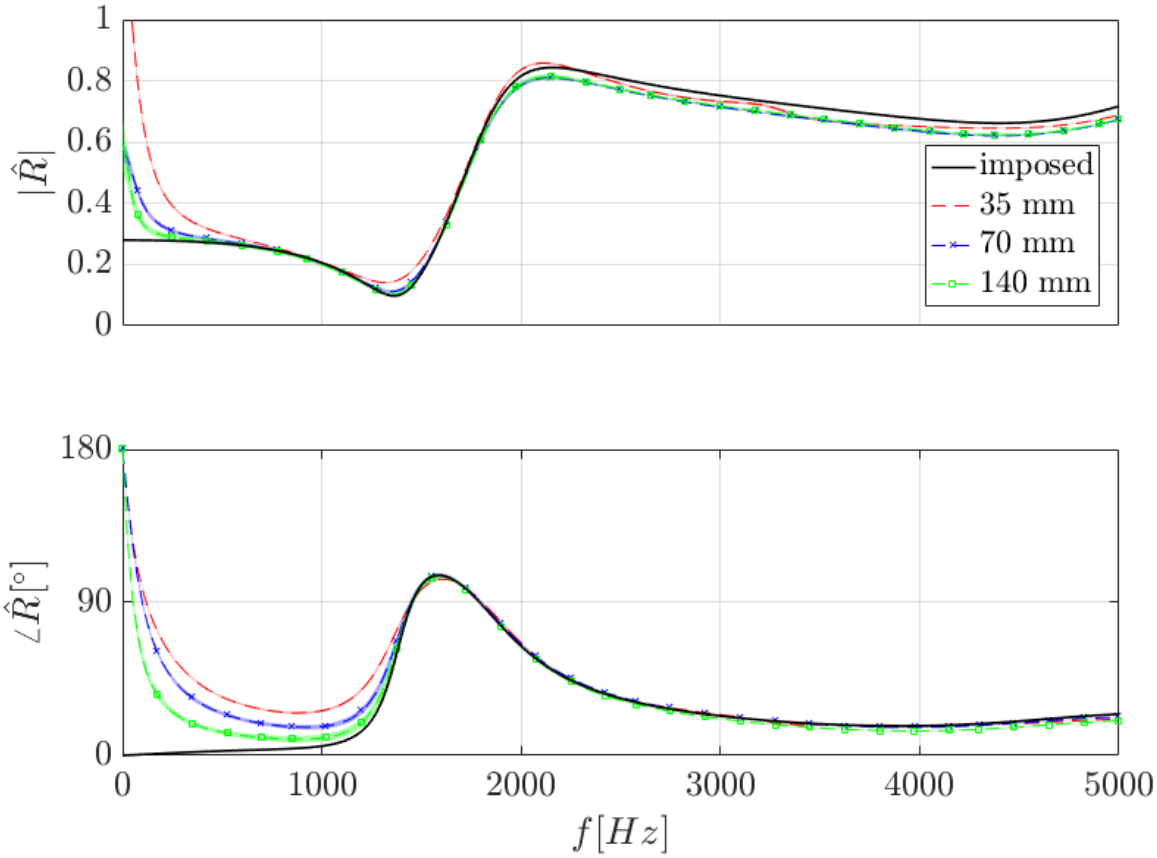

Figure E.1: Comparison of the estimated and imposed reflection coefficient on the outlet for various duct lengths.

It shows, that a longer duct length results in higher accordance of imposed and measured reflection coefficient at low frequencies. However, a even in this case the measured reflection coefficient differs considerably from the imposed curve towards low frequencies. Calculation time increases considerably with higher duct length. When using the same excitation signal amplitude as for the 35 and 70 mm test case, the amplitude of the f wave decreases significantly during the propagation from the inlet to the outlet. The small amplitude values result in a large offset between imposed and measured reflection coefficient at the outlet in this case. To prevent this, the amplitude of the excitation signal has to be increased.

Therefore, increasing the duct length is not an acceptable solution for the problem of divergence between measured and imposed reflection coefficient at low frequencies.

F Operating pressure

Numerical round-off error occurs especially when calculating the pressure in low-Mach-number compressible flow. This is the result of the small relative size of the overall pressure drop Δp in comparison to the absolute static pressure p. The pressure change Δp is proportional to the dynamic head $\frac{1}{2}\gamma p M^2$, where γ designates the ratio of specific heat capacities at constant pressure and constant volume $\frac{c_p}{c_V}$. M is the Mach number with $M \ll 1$. This yields the relation

$$\frac{\Delta p}{p} \sim M^2 \tag{F.1}$$

and therefore $\frac{\Delta p}{p} \rightarrow 0$ for $M \rightarrow 0$. This shows the need for taking measures to reduce the round-off error in the pressure calculation in low-Mach-number flow. In Fluent, the problem of round-off error is significantly reduced by diminishing the absolute pressure p_{abs} by the operating pressure p_{op}

$$p_{gauge} = p_{abs} - p_{op}, \tag{F.2}$$

whereas the resulting pressure is defined as the gauge pressure. The operating pressure is usually of a level similar to the absolute pressure in the flow. the default value for the operating pressure is $101325Pa$. Pressure input and output variables in Fluent are always gauge pressures. The significance of setting an adequate operating pressure can be explained by the direct link between the computation of the density by the ideal incompressible gas law

$$\rho = \frac{p_{op}}{\frac{R_{univ}}{M_w} T}, \tag{F.3}$$

whereas R_{univ} is the universal gas constant and M_w designates the mean molecular weight of the material. For high-Mach-number compressible flows, it is recommended not to use an operating pressure, because the pressure changes are significant and round-off error is thus strongly limited. In these cases, the user manual suggests to set the operating pressure to zero, in order to equalize gauge and absolute pressure [5].

Bibliography

[1] ANSYS, Inc., Canonsburg, PA 15317, USA. *ANSYS® Academic Research, Release 16.2, Help System, Euler Equations*, 2016.

[2] ANSYS, Inc., Canonsburg, PA 15317, USA. *ANSYS® Academic Research, Release 16.2, Help System, Flow Solvers*, 2016.

[3] ANSYS, Inc., Canonsburg, PA 15317, USA. *ANSYS® Academic Research, Release 16.2, Help System, General Non-Reflecting Boundary Conditions*, 2016.

[4] ANSYS, Inc., Canonsburg, PA 15317, USA. *ANSYS® Academic Research, Release 16.2, Help System, Impedance Boundary Conditions*, 2016.

[5] ANSYS, Inc., Canonsburg, PA 15317, USA. *ANSYS® Academic Research, Release 16.2, Help System, The Effect of Numerical Roundoff on Pressure Calculation in Low-Mach-Number Flow*, 2016.

[6] L. Tay Wo Chong, T. Komarek, R. Kaess, S. Föller, and W. Polifke. Identification of flame transfer functions from LES of a premixed swirl burner. In *Proceedings of ASME Turbo Expo 2010: Power for Land, Sea and Air*, Glasgow, UK, 6 2010. ASME.

[7] K. Förner and W. Polifke. Nonlinear aeroacoustic characterization of Helmholtz resonators with a local-linear neuro-fuzzy network model. *Journal of Sound and Vibration*, 407(Supplement C):170 – 190, 2017.

[8] T. J. Poinsot and S. K. Lele. Boundary conditions for direct simulations of compressible viscous flows. *Journal of Computational Physics*, 101(1):104 – 129, 1992.

[9] T. D. Jadhav, A. Khondge, V. Ivanov, B. Makarov, and C. Hill. Broadband model for impedance boundary condition in a Navier-Stokes solver. In *20th AIAA/CEAS Aeroacoustics Conference, AIAA AVIATION Forum, (AIAA 2014-2742)*, 2014.

[10] S. Jaensch, C. Sovardi, and W. Polifke. On the robust, flexible and consistent implementation of time domain impedance boundary conditions for compressible flow simulations. *Journal of Computational Physics*, 314:145 – 159, 2016.

[11] R. M. Kulkarni and W. Polifke. LES of delft-jet-in-hot-coflow (DJHC) with tabulated chemistry and stochastic fields combustion model. *Fuel Processing Technology*, 107(Supplement C):138 – 146, 2013. Selected Papers from the Eleventh International Conference on Combustion and Energy Utilization (11th ICCEU).

[12] L. Ljung. System identification. In *Signal analysis and prediction*, pages 163–173. Springer, 1998.

[13] The MathWorks, Inc., Natick, MA 01760, USA. *MATLAB® and System Identification Toolbox, Release R2016a*, 2016.

[14] W. Polifke. System identification for aero- and thermo-acoustic applications. In C. Schram, editor, *Advances in Aero-Acoustics and Thermo-Acoustics*, pages 1–46. Von Karman Institute, Rhode-Saint-Genèse, Belgium, 2011.

[15] W. Polifke. Black-box system identification for reduced order model construction. *Annals of Nuclear Energy*, 67(Supplement C):109 – 128, 2014. Advanced stability analysis for nuclear reactors.

[16] W. Polifke, C. Wall, and P. Moin. Partially reflecting and non-reflecting boundary conditions for simulation of compressible viscous flow. *Journal of Computational Physics*, 213(1):437 – 449, 2006.

[17] S. Schmidt. Gas dynamics. Lecture manuscript, Chair of Aerodynamics and Fluid Mechanics, Technical University of Munich, 2011.

[18] A. Sharma. *Essentials of Fluid-Dynamics and Heat-Transfer for CFD*, pages 41–71. John Wiley and Sons, Ltd, 2016.

[19] C. F. Silva, W. Polifke, J. O'Brien, and M. Ihme. Towards concurrent identification of flame dynamics and combustion noise of enclosed flames. In C. Schram, editor, *Proceedings of the Summer Program 2014*, pages 179 – 188. Center for Turbulence Research, Stanford, CA 94305, USA, 2014.

[20] C. Sovardi, S. Jaensch, and W. Polifke. Concurrent identification of aero-acoustic scattering and noise sources at a flow duct singularity in low mach number flow. *Journal of Sound and Vibration*, 377:90 – 105, 2016.

[21] P. Testud, Y. Aurégan, P. Moussou, and A. Hirschberg. The whistling potentiality of an orifice in a confined flow using an energetic criterion. *Journal of Sound and Vibration*, 325(4):769 – 780, 2009.

[22] P. Tudisco, R. Ranjan, S. Menon, S. Jaensch, and W. Polifke. Application of the time-domain impedance boundary condition to large-eddy simulation of combustion instability in a shear-coaxial high pressure combustor. *Flow, Turbulence and Combustion*, 99(1):185–207, Jul 2017.

[23] M. P. G. Zellhuber. *High Frequency Response of Auto-Ignition and Heat Release to Acoustic Perturbations*. PhD thesis, Technical University of Munich, 2013.